6-8-93
E-7656

NASA Technical Memorandum 106055
ICOMP–93–05

Positivity-Preserving Numerical Schemes for Multidimensional Advection

B.P. Leonard
Institute for Computational Mechanics in Propulsion
Lewis Research Center
Cleveland, Ohio

and

M.K. MacVean and A.P. Lock
U.K. Meteorological Office
Atmospheric Processes Research Division
Bracknell, England

March 1993

NASA

INSTITUTE FOR COMPUTATIONAL MECHANICS IN PROPULSION
NASA Lewis Research Center
ICOMP
Case Western Reserve University
Ohio Aerospace Institute

Positivity-Preserving Numerical Schemes for Multidimensional Advection

B.P. Leonard
*Institute for Computational Mechanics in Propulsion**
Lewis Research Center
Cleveland, Ohio 44135

M.K. MacVean and A.P. Lock
U.K. Meteorological Office
Atmospheric Processes Research Division
Bracknell, England

SUMMARY

This report describes the construction of an explicit, single time-step, conservative, finite-volume method for multidimensional advective flow, based on a uniformly third-order polynomial interpolation algorithm (UTOPIA). Particular attention is paid to the problem of flow-to-grid angle-dependent, anisotropic distortion typical of one-dimensional schemes used component-wise. The third-order multidimensional scheme automatically includes certain cross-difference terms that guarantee good isotropy (and stability). However, above first-order, polynomial-based advection schemes do not preserve positivity (the multidimensional analogue of monotonicity). For this reason, a multidimensional generalisation of the first author's universal flux-limiter is sought. This is a very challenging problem. A simple flux-limiter can be found; but this introduces strong anisotropic distortion. A more sophisticated technique, limiting part of the flux and then restoring the isotropy-maintaining cross-terms afterwards, gives more satisfactory results. Test cases are confined to two dimensions; three-dimensional extensions are briefly discussed.

INTRODUCTION

Many numerical models in computational fluid dynamics employ so-called ''leap-frog'' finite-difference schemes using second-order centred differences in both time and space. One significant attribute of such methods is that for purely advective flow there is no artificial dissipation supplied from the numerical scheme. This has both positive and negative consequences. On the one hand, where the flow is well resolved, the numerical

*Work funded under NASA Cooperative Agreement NCC3-233.

method does not corrupt modelled physical diffusivity or viscosity. However, it is well known that in the presence of sharp changes in gradient, centred schemes exhibit serious phase errors generating spurious oscillations and unphysical maxima and minima in the transported variables. And because of the lack of inherent numerical dissipation, these oscillations are not strongly damped and may lead to unnatural processes such as ''numerical turbulence'' thereby producing anomalous mixing. First-order methods are nonoscillatory, but contain too much inherent artificial diffusivity to be seriously considered as the basis for a multidimensional advection scheme. By contrast, third-order upwind schemes possess the inherent stability of upwinding in addition to high accuracy and excellent phase behaviour, although small unphysical undershoots or overshoots may still be excited in sharp-gradient regions. The current work focuses on the development of an explicit, single-time-step, conservative, flux-based, control-volume algorithm for multidimensional advection. This is in contrast to the common practice of operator-splitting (using locally one-dimensional algorithms) which, by its nature, cannot be formulated in a conservative manner.

One other aspect of multidimensional advection schemes that has received little attention is the problem of anisotropic distortion that occurs when advection is oblique or skew to the grid lines. The problem stems from using one-dimensional advection formulae in each coordinate direction separately, without explicitly taking account of necessary cross-difference terms. In practical simulations of physical processes, the effects of this distortion are not generally immediately apparent because the flow patterns are very complex and the true solution is not normally known. However, simple model test problems (with known solutions) of advection oblique to the grid suggest that serious quantitative errors may be introduced through this mechanism in some circumstances. It should be noted that the commonly used test problem of advection of an initial profile around a circular path does not highlight this type of distortion because the flow-to-grid angle is continuously changing. But in a relatively constant-direction flow field, this problem can evidently lead to quite substantial errors. In addition, above first-order, one-dimensional schemes used component-wise for multidimensional pure advection are unconditionally unstable (unless the flow is aligned with the grid). This is usually a weak long-wavelength instability and is often not excited in spatially varying velocity fields. Although a small amount of physical diffusion is usually enough to suppress the instability, an advectively stable algorithm seems more desirable.

A number of one-dimensional monotonicity-preserving (MP) advection schemes have recently been compared (Bull, 1990). Schemes tested include a second-order total-variation-diminishing (TVD) flux-limited scheme due to van Leer (1974), referred to as the curved-line advection method (CLAM), and Leonard's (1991) ULTIMATE QUICKEST algorithm, a third-order one-dimensional MP advection scheme. These methods have also been tested in two dimensions with explicit forward time-stepping using fluxes based on the one-dimensional formulae in each coordinate direction. Although the CLAM scheme maintains ''positivity'' (the multidimensional analogue of monotonicity) provided the Courant number is small enough, the one-dimensional ULTIMATE scheme, applied coordinate-wise does not. In addition, both methods generate strong anisotropic distortion, although of a different type to that observed with unlimited centred differences.

The following sections address the two outstanding problems of (i): eliminating anisotropic distortion and (ii): developing a truly multidimensional flux-limiting strategy. The proposed techniques are tested on a conceptually simple but numerically very

challenging problem involving pure two-dimensional advection of an initial circularly symmetric Gaussian profile by a constant velocity field oblique to a uniform square mesh. An angle of 45° usually gives worst-case distortion; however, other angles are also considered in order to develop some perspective on flow-to-grid angle dependence. All of the test cases and most of the discussion will be confined to two dimensions. Although there is a large theoretical gap to be bridged between one and two dimensions, it appears that, once this is achieved, algorithmic extension to three dimensional advection may be relatively straight-forward.

ELIMINATION OF ANISOTROPIC DISTORTION

Anisotropic distortion appears in multidimensional advection schemes that rely on the respective one-dimensional formulae in each coordinate direction separately. As a result of this, computed solutions are strongly dependent on the flow-to-grid angle; equivalently, this means that solutions are not grid-orientation independent. This problem can be seen theoretically by making use of the two-dimensional complex amplitude ratio (or amplification factor) **G**. For reference, consider a model two-dimensional advection-diffusion equation for a scalar $\phi(x,y,t)$

$$\frac{\partial \phi}{\partial t} + u\frac{\partial \phi}{\partial x} + v\frac{\partial \phi}{\partial y} = D\left(\frac{\partial^2 \phi}{\partial x^2} + \frac{\partial^2 \phi}{\partial y^2}\right) \tag{1}$$

where u, v, and D are *constant* coefficients. It is of interest to follow the evolution of a wave of the form

$$\phi = \mathbf{A}(t)\exp(\iota k_x x)\exp(\iota k_y y) \tag{2}$$

involving component wave-numbers k_x and k_y, where $\mathbf{A}(t)$ is the (complex) amplitude and ι (iota) represents the imaginary unit, $\sqrt{-1}$. The complex amplitude ratio **G** is then defined as

$$\mathbf{G} = \frac{\phi(x,\ y,\ t+\Delta t)}{\phi(x,\ y,\ t)} = \frac{\mathbf{A}(t+\Delta t)}{\mathbf{A}(t)} \tag{3}$$

Substitution of (2) into (1) gives

$$\phi = \mathrm{A}(0)\exp[-(k_x^2+k_y^2)Dt]\exp[\iota k_x(x-ut)]\exp[\iota k_y(y-vt)] \tag{4}$$

so that the *exact* expression for the two-dimensional **G** of the model advection-diffusion equation is

$$\mathbf{G}_{\mathrm{exact}} = \exp[-(\alpha_x\theta_x^2+\alpha_y\theta_y^2)]\exp(-\iota c_x\theta_x)\exp(-\iota c_y\theta_y) \tag{5}$$

where the diffusion parameters

$$\alpha_x = \frac{D\Delta t}{\Delta x^2} \tag{6}$$

and

$$\alpha_y = \frac{D\Delta t}{\Delta y^2} \tag{7}$$

and component Courant numbers

$$c_x = \frac{u\Delta t}{\Delta x} \tag{8}$$

and

$$c_y = \frac{v\Delta t}{\Delta y} \tag{9}$$

have been introduced, and the nondimensional wave-numbers are given by

$$\theta_x = k_x \Delta x \tag{10}$$

and

$$\theta_y = k_y \Delta y \tag{11}$$

For purely advective flow in two dimensions, $D = 0$ and (5) becomes

$$\mathbf{G}_{\mathrm{adv}} = \exp[-\iota(c_x\theta_x + c_y\theta_y)] \tag{12}$$

A Taylor expansion of real and imaginary parts of this expression gives, to third order in θ_x and θ_y,

$$\mathbf{G}_{\mathrm{adv}} = 1 - \left[\frac{1}{2}c_x^2\theta_x^2 + c_x\theta_x c_y\theta_y + \frac{1}{2}c_y^2\theta_y^2\right] + \ldots$$

$$- \iota\left[(c_x\theta_x + c_y\theta_y) - \frac{1}{6}(c_x\theta_x + c_y\theta_y)^3 + \ldots\right] \tag{13}$$

The corresponding numerical **G** for a given computational method (involving a single forward time-step) can be similarly expanded in a Taylor series. It is not difficult to see that the use of only one-dimensional advective formulae in each coordinate direction would result in a **G**-expansion involving powers of $(c_x\theta_x)$ and $(c_y\theta_y)$ separately, but no cross-terms. In particular, the important second-order term

$$(c_x\theta_x)(c_y\theta_y) \tag{14}$$

appearing in (13), is absent from such schemes. Thus, flow along coordinate directions (either $c_x = 0$ or $c_y = 0$) may be well modelled, but at other angles the missing term will clearly lead to errors. One might expect most distortion to occur for flow along grid-diagonals (i.e., at 45° on a uniform square mesh), and this is in fact borne out by numerical experiments.

As will be shown, it is possible to devise an explicit, forward-time-step, conservative control-volume formulation of advective transport that includes all the terms (through third order) involved in (13). It is also a straight-forward matter to generalise the method to three

dimensions (see Appendix 1), and to extend the theory to include diffusion terms to the same order (Appendix 2). This uniformly third-order multidimensional scheme is not, however, positivity preserving. Rather, it is the analogue of the third-order one-dimensional QUICKEST scheme (Leonard, 1979), which also generates (albeit relatively small) overshoots or undershoots when modelling sharp changes in gradient. In the one-dimensional case, a rather simple universal limiter (valid for any order of accuracy) can be applied, resulting in the monotonicity-preserving ULTIMATE QUICKEST scheme (Leonard, 1991). The extension of the limiting strategy to two (and three) dimensions is by no means straightforward; however, some progress has been made, and this is described in the next section. The remainder of this section is devoted to studying anisotropic distortion of unlimited schemes and to the description of the two-dimensional uniformly third-order advection method.

A simple test problem has been set up to study anisotropic distortion under purely advective conditions. This consists of a uniform square grid ($\Delta x = \Delta y = h$) over a 31×31 domain (i.e., $h = 1/31$) with a uniform velocity field at an angle Θ to the x-axis

$$\mathbf{V} = (u, v) = (V_0 \cos\Theta, V_0 \sin\Theta) \tag{15}$$

The problem simulates the equation

$$\frac{\partial \phi}{\partial t} + \mathbf{V} \cdot \nabla \phi = 0 \tag{16}$$

representing pure advection of a simple scalar "density" profile, $\phi(x,y,t)$, taken here to be a circularly symmetric Gaussian distribution with a standard deviation of $3h$, initially established at the centre of the grid. The domain has doubly periodic boundary conditions so that the profile can be advected any distance, depending on the run time. In most cases, Θ is chosen to be 45° ($c_x = c_y$), and Δt is adjusted so that the (exact-solution) profile would be advected a distance $31\sqrt{2}\,h$; i.e., to the centre of the next diagonal "box". This is shown schematically for the exact solution in Figure 1(a), giving contours of constant density. Figure 1(b) shows a "three-dimensional" portrayal of the initial ($\equiv$ final) distribution. Of course, the actual computation takes place within a single box, with the profile "exiting" at the top-right corner and "re-entering" at the lower-left, with the final position at the center again. For the 45° case, $c_x = c_y = 31/N$, where N is the number of time steps.

By contrast to the exact solution of Figure 1, Figure 2 shows the results of using the ("standard") space-time-centred leap-frog scheme,

$$\phi_{i,j}^{n+1} = \phi_{i,j}^{n-1} - c_x(\phi_{i+1,j}^{n} - \phi_{i-1,j}^{n}) - c_y(\phi_{i,j+1}^{n} - \phi_{i,j-1}^{n}) \tag{17}$$

for $c_x = c_y = 0.25$ ($N = 124$). Clearly, even for this relatively smooth initial profile, there has been significant anisotropic distortion in addition to serious (phase-lag) oscillations due to the inherent (undamped) numerical dispersion, characteristic of this scheme. The second-order (three time-level) leap-frog scheme gives results showing similar distortion to that of a method using the (two time-level) explicit one-dimensional Lax-Wendroff (1960) scheme in each coordinate direction separately,

$$\phi_{i,j}^{n+1} = \phi_{i,j}^{n} - c_x\left[\frac{1}{2}(\phi_{i+1,j}^{n} - \phi_{i-1,j}^{n}) - \frac{c_x}{2}(\phi_{i+1,j}^{n} - 2\phi_{i,j}^{n} + \phi_{i-1,j}^{n})\right]$$

$$- c_y\left[\frac{1}{2}(\phi_{i,j+1}^{n} - \phi_{i,j-1}^{n}) - \frac{c_y}{2}(\phi_{i,j+1}^{n} - 2\phi_{i,j}^{n} + \phi_{i,j-1}^{n})\right] \tag{18}$$

This scheme is unconditionally *un*stable unless the flow is aligned with one of the coordinate directions. However, for small time-steps, the instability is weak, and results can be obtained over short run-times, as shown in Figure 3. Again, significant distortion and phase-lag oscillations are immediately obvious. For extended run-times, the computation will ultimately ''blow-up''.

As in the one-dimensional case, oscillations can be avoided by reverting to a first-order upwind technique. If one employs a simple-minded, coordinate-wise one-dimensional scheme (for c_x and c_y both positive)

$$\phi_{i,j}^{n+1} = \phi_{i,j}^{n} - c_x(\phi_{i,j}^{n} - \phi_{i-1,j}^{n}) - c_y(\phi_{i,j}^{n} - \phi_{i,j-1}^{n}) \tag{19}$$

the results are as shown in Figure 4 for $c_x = c_y = 0.5$. In this case there are no undershoots (this is the simplest two-dimensional positivity-preserving advection scheme). However, gross anisotropic distortion is observed, as is a massive loss in peak value. Both of these effects are due to the large amount of artificial numerical diffusion inherent in this method. Figure 5 shows the diamond-shaped von Neumann stability region in the (c_x, c_y) plane for first-order upwinding used coordinate-wise, allowing for positive or negative velocity components; i.e., $|c_x| + |c_y| \leq 1$.

Equation (19) can be rewritten as a conservative, control-volume, explicit update equation

$$\phi_{i,j}^{n+1} = \phi_{i,j}^{n} + \mathrm{FLUXW}(i, j) - \mathrm{FLUXW}(i+1, j)$$

$$+ \mathrm{FLUXS}(i, j) - \mathrm{FLUXS}(i, j+1) \tag{20}$$

by identifying the west-face advective flux (for $c_x > 0$) as

$$\mathrm{FLUXW}(i, j) = c_x \phi_w = c_x \phi_{i-1,j}^{n} \tag{21}$$

and the south-face flux (for $c_y > 0$) as

$$\mathrm{FLUXS}(i, j) = c_y \phi_s = c_y \phi_{i,j-1}^{n} \tag{22}$$

where ϕ_w and ϕ_s are considered to be the effective west and south face-values, respectively, advected into a given control volume. Note that (20) guarantees conservation by expressing the east-face flux in terms of the west-face flux at control-volume $(i+1, j)$, and similarly for the north-face flux in terms of the south-face of $\mathrm{CV}(i, j+1)$. This simple type of first-order upwinding assumes that the scalar value advected across any particular face is effectively equal to the immediate upwind node-value in a direction normal to that face. But this does not take account of the fact that, in general, the advective flux is sweeping across the face at an angle (rather than simply in the normal direction). Figure 6 suggests that the (upwind-biased) *transverse gradient* of ϕ should be important in this respect. In fact, if one assumes that in the vicinity of the west face, the scalar value varies linearly between $\phi_{i-1,j}^{n}$ and

$\phi^n_{i-1,j-1}$, it is not difficult to show that the corresponding average face-value (over a time-step Δt) is

$$\phi_w = \phi^n_{i-1,j} - \frac{c_y}{2}(\phi^n_{i-1,j} - \phi^n_{i-1,j-1}) \tag{23}$$

thus differing from the simple-minded upwind formula by the appearance of the *transverse-gradient* term (for c_x, $c_y > 0$)

$$\text{GRADTW} = \phi^n_{i-1,j} - \phi^n_{i-1,j-1} \tag{24}$$

Similarly, the south-face value can be shown to be

$$\phi_s = \phi^n_{i,j-1} - \frac{c_x}{2}\,\text{GRADTS} \tag{25}$$

where (again for c_x, $c_y > 0$)

$$\text{GRADTS} = \phi^n_{i,j-1} - \phi^n_{i-1,j-1} \tag{26}$$

When these formulae are used in (20), the results are as shown in Figure 7. By comparison with Figure 4, it is immediately obvious that inclusion of the transverse-gradient terms has restored isotropy (at least for $\Theta = 45°$), although there is still significant artificial diffusion as evidenced by the strong loss in peak value and concomitant spreading. At other advection angles there is some anisotropic distortion, but not nearly as much as with the simple first-order scheme of (19). The von Neumann stability region in the (c_x, c_y) plane is now a square: $(1-|c_x|)(1-|c_y|) \geq 0$. Also note that *exact* point-to-point transfer occurs (across a grid diagonal) when $|c_x| = |c_y| = 1$.

Inclusion of the GRADT terms can be directly related to the appearance of the second-order cross-term $(c_x\theta_x)(c_y\theta_y)$ in the Taylor expansion of the numerical complex amplitude ratio. Thus it would appear that the two-dimensional, conservative, flux-based, control-volume formulation of the Lax-Wendroff scheme would benefit from inclusion of these terms, as well. This is suggested in Figure 8, where it is assumed that ϕ has a linear dependence on both x and y in the vicinity of the west face, collocated (at time-level n) at $\phi^n_{i,j}$, $\phi^n_{i-1,j}$, and $\phi^n_{i-1,j-1}$ (for c_x and c_y both positive). Clearly from the figure, these are the appropriate (upwind-biased) nodes. Taking the time average (over Δt) of the west-face value (equivalent to averaging ϕ^n over the area covered by the small angled arrows) then leads to

$$\phi_w = \frac{1}{2}(\phi^n_{i,j} + \phi^n_{i-1,j}) - \frac{c_x}{2}(\phi^n_{i,j} - \phi^n_{i-1,j}) - \frac{c_y}{2}(\phi^n_{i-1,j} - \phi^n_{i-1,j-1}) \tag{27}$$

where one again sees the appearance of the GRADTW term, defined in (24). The corresponding south-face value (for c_x and c_y both positive) is

$$\phi_s = \frac{1}{2}(\phi^n_{i,j} + \phi^n_{i,j-1}) - \frac{c_y}{2}(\phi^n_{i,j} - \phi^n_{i,j-1}) - \frac{c_x}{2}(\phi^n_{i,j-1} - \phi^n_{i-1,j-1}) \tag{28}$$

It should be clear that the GRADT terms are dependent on the signs of both c_x and c_y, although the other (face-centred) terms in (27) and (28) are independent of the signs of the respective advecting velocity components. The results of using (27) and (28) in (20) are

shown in Figure 9 for $c_x = c_y = 0.25$. This is clearly an improvement over Figure 3, although there is still a large degree of phase-lag dispersion (just as in the one-dimensional case). The Taylor expansion of the numerical **G** corresponding to this scheme matches (13) identically through all *second*-order terms (including the $c_x\theta_x c_y\theta_y$ cross-term). Thus it can be considered to be the two-dimensional, conservative, control-volume analogue of the Lax-Wendroff scheme. Inclusion of the transverse-gradient terms also restores stability; the stable region is once again the square: $(1-|c_x|)(1-|c_y|) \geq 0$. Extension to three dimensions is straight-forward, simply involving an additional transverse-gradient term (along the extra coordinate direction) in the formulae for each of the *three* face-values. Incorporation of standard second-order differences for diffusive fluxes is consistent with the Taylor expansion of (5) involving all second-order combinations of the α's and c's.

Flux-Based Formulation

It is instructive to re-derive the uniformly second-order advection scheme from a rather different view-point. This will suggest a way of generalising to uniformly third (and potentially higher) order methods. The idea is based on the fact that for pure advection at a constant velocity **V**, the scalar value at a point **x** at the new time-level is equal to that at position $\mathbf{x}-\mathbf{V}\Delta t$ evaluated at a time Δt earlier:

$$\phi(\mathbf{x},\ t+\Delta t) \quad = \quad \phi(\mathbf{x}-\mathbf{V}\Delta t,\ t) \tag{29}$$

This means that ϕ can be predicted at any given (nodal) point by projecting back along an advective characteristic and interpolating spatially to evaluate ϕ at the *origination point* at the earlier time-level. The accuracy of the scheme then depends entirely on the form of the *spatial* interpolation used for evaluation of the right-hand side of (29). Although the algorithm is derived on the basis of a constant **V**, the update algorithm is subsequently rewritten in a flux-based, conservative control-volume form, wherein the individual advecting face velocities are allowed to be spatially varying in conformity with a solenoidal velocity field.

Referring to Figure 10, assume that at the earlier time-level

$$\phi(x,\ y,\ t) \quad = \quad \phi^n(\xi,\ \eta) \tag{30}$$

where ξ and η are local x- and y-coordinates centered in the control volume. In the case shown (c_x, $c_y > 0$), assume that

$$\phi^n(\xi,\eta) \quad = \quad C_1 + C_2\,\xi + C_3\,\xi^2 + C_4\,\eta + C_5\,\eta^2 + C_6\,\xi\,\eta \tag{31}$$

and evaluate the C's by collocating at the six node-values. Note that the inclusion of the $(i-1,\ j-1)$-node gives the appropriate upwind bias in the quadrant corresponding to the position of the origination point (shown by the circled star). It should be clear how the stencil changes for origination points in other quadrants.

It is not difficult to show that the C's are given by

$$C_1 = \phi^n_{i,j} \tag{32}$$

$$C_2 = \frac{(\phi^n_{i+1,j} - \phi^n_{i-1,j})}{2\Delta x} \tag{33}$$

$$C_3 = \frac{(\phi^n_{i+1,j} - 2\phi^n_{i,j} + \phi^n_{i-1,j})}{2\Delta x^2} \tag{34}$$

$$C_4 = \frac{(\phi^n_{i,j+1} - \phi^n_{i,j-1})}{2\Delta y} \tag{35}$$

$$C_5 = \frac{(\phi^n_{i,j+1} - 2\phi^n_{i,j} + \phi^n_{i,j-1})}{2\Delta y^2} \tag{36}$$

and

$$C_6 = \frac{(\phi^n_{i,j} - \phi^n_{i-1,j} - \phi^n_{i,j-1} + \phi^n_{i-1,j-1})}{\Delta x\,\Delta y} \tag{37}$$

The upwind bias of the latter coefficient, of course, depends on the signs of c_x and c_y, whereas the other coefficients are centred with respect to node (i, j). It is easy to see how C_6 would change for the three other combinations of signs of c_x and c_y.

From (29) and (30), the explicit update formula can be written in general as

$$\phi^{n+1}_{i,j} = \phi^n(-u\Delta t,\ -v\Delta t) \tag{38}$$

For the particular (second-order) case shown in Figure 10, substituting the above C-values results in

$$\begin{aligned}\phi^{n+1}_{i,j} = \phi^n_{i,j} &- \frac{c_x}{2}(\phi^n_{i+1,j} - \phi^n_{i-1,j}) + \frac{c_x^2}{2}(\phi^n_{i+1,j} - 2\phi^n_{i,j} + \phi^n_{i-1,j}) \\ &- \frac{c_y}{2}(\phi^n_{i,j+1} - \phi^n_{i,j-1}) + \frac{c_y^2}{2}(\phi^n_{i,j+1} - 2\phi^n_{i,j} + \phi^n_{i,j-1}) \\ &+ c_x c_y(\phi^n_{i,j} - \phi^n_{i-1,j} - \phi^n_{i,j-1} + \phi^n_{i-1,j-1})\end{aligned} \tag{39}$$

This can be rewritten in conservative control-volume form, as given by (20), by identifying west and south face-values as, respectively,

$$\phi_w = \frac{1}{2}(\phi^n_{i,j} + \phi^n_{i-1,j}) - \frac{c_x}{2}(\phi^n_{i,j} - \phi^n_{i-1,j}) - \frac{c_y}{2}\mathrm{GRADTW} \tag{40}$$

and

$$\phi_s = \frac{1}{2}(\phi^n_{i,j} + \phi^n_{i,j-1}) - \frac{c_y}{2}(\phi^n_{i,j} - \phi^n_{i,j-1}) - \frac{c_x}{2}\text{GRADTS} \tag{41}$$

where GRADTW and GRADTS are given (for c_x, $c_y > 0$) by (24) and (26), respectively. These face-values are identical to those given by (27) and (28)—i.e., the one-dimensional Lax-Wendroff formulae together with the appropriate (upwind-biased) GRADT terms. Note particularly how the cross-difference term, given by the last term in (39), has been split between x- and y-fluxes. This is made possible because of the identity

$$(\phi_{i,j} - \phi_{i-1,j}) - (\phi_{i,j-1} - \phi_{i-1,j-1}) \equiv (\phi_{i,j} - \phi_{i,j-1}) - (\phi_{i-1,j} - \phi_{i-1,j-1}) \tag{42}$$

corresponding to the cross-derivative identity

$$\frac{\partial^2\phi}{\partial y\,\partial x} \equiv \frac{\partial^2\phi}{\partial x\,\partial y} \tag{43}$$

This type of manipulation is particularly important in developing higher-order formulae, such as the uniformly third-order method considered next. It should also be noted from (39) that exact nodal point-to-point transfer occurs when $c_x = 1$ and $c_y = 0$ (or *vice versa*), and also (across the grid diagonal) when $c_x = c_y = 1$, when GRADT-terms are included.

Uniformly Third Order Polynomial Interpolation Algorithm

Figure 11 shows the appropriate upwind-biased 10-point stencil for collocating a third-order polynomial of the form

$$\begin{aligned}\phi^n(\xi,\eta) = {} & C_1 + C_2\,\xi + C_3\,\xi^2 + C_4\,\xi^3 \\ & + C_5\,\eta + C_6\,\xi\,\eta + C_7\,\xi^2\,\eta \\ & + C_8\,\eta^2 + C_9\,\xi\,\eta^2 \\ & + C_{10}\,\eta^3\end{aligned} \tag{44}$$

For notational convenience the subscripts on the node-values denote central-point (P), west (W), east (E), north (N), south (S), north-west (NW), double-west (WW), etc. (as usual, capital letters are used for node-values and lower-case for face-values); the time-level n superscript has also been dropped. In Figure 11, the collocation points have been chosen so as to give some upwind bias corresponding to the location of the origination point. Also note the symmetry of the stencil about a diagonal closest in direction to that of the advecting velocity vector. (It should be clear how the stencil changes for location of the origination point in other quadrants). For this choice of stencil, it is not difficult to derive the following

C-values:

$$C_1 = \phi_P \tag{45}$$

$$C_2 = \frac{(\phi_E - \phi_W)}{2\Delta x} - \frac{(\phi_E - 3\phi_P + 3\phi_W - \phi_{WW})}{6\Delta x} \tag{46}$$

$$C_3 = \frac{(\phi_E - 2\phi_P + \phi_W)}{2\Delta x^2} \tag{47}$$

$$C_4 = \frac{(\phi_E - 3\phi_P + 3\phi_W - \phi_{WW})}{6\Delta x^3} \tag{48}$$

$$C_5 = \frac{(\phi_N - \phi_S)}{2\Delta y} - \frac{(\phi_N - 3\phi_P + 3\phi_S - \phi_{SS})}{6\Delta y} \tag{49}$$

$$C_6 = \frac{(\phi_E - \phi_P) - (\phi_{SE} - \phi_S) + (\phi_N - \phi_{NW}) - (\phi_P - \phi_W)}{2\Delta x\,\Delta y} \tag{50}$$

$$C_7 = \frac{(\phi_E - \phi_{SE}) - 2(\phi_P - \phi_S) + (\phi_W - \phi_{SW})}{2\Delta x^2\,\Delta y} \tag{51}$$

$$C_8 = \frac{(\phi_N - 2\phi_P + \phi_S)}{2\Delta y^2} \tag{52}$$

$$C_9 = \frac{(\phi_N - \phi_{NW}) - 2(\phi_P - \phi_W) + (\phi_S - \phi_{SW})}{2\Delta x\,\Delta y^2} \tag{53}$$

and

$$C_{10} = \frac{(\phi_N - 3\phi_P + 3\phi_S - \phi_{SS})}{6\Delta y^3} \tag{54}$$

Substitution of these values into (44) and (38) results in the following formula for the updated (superscript +) central-point node-value:

$$\begin{aligned}
\phi_P^+ = \phi_P &- \frac{c_x}{2}(\phi_E - \phi_W) + \frac{c_x(1 - c_x^2)}{6}(\phi_E - 3\phi_P + 3\phi_W - \phi_{WW}) \\
&- \frac{c_y}{2}(\phi_N - \phi_S) + \frac{c_y(1 - c_y^2)}{6}(\phi_N - 3\phi_P + 3\phi_S - \phi_{SS}) \\
&+ \frac{c_x^2}{2}(\phi_E - 2\phi_P + \phi_W) + \frac{c_y^2}{2}(\phi_N - 2\phi_P + \phi_S) \\
&+ \frac{c_x c_y}{2}\left[(\phi_E - \phi_P) - (\phi_{SE} - \phi_S) + (\phi_N - \phi_{NW}) - (\phi_P - \phi_W)\right] \\
&- \frac{c_x c_y^2}{2}\left[(\phi_N - \phi_{NW}) - 2(\phi_P - \phi_W) + (\phi_S - \phi_{SW})\right] \\
&- \frac{c_x^2 c_y}{2}\left[(\phi_E - \phi_{SE}) - 2(\phi_P - \phi_S) + (\phi_W - \phi_{SW})\right]
\end{aligned} \tag{55}$$

This can be written in conservative control-volume form by identifying the *effective* advected west-face value as

$$\begin{aligned}
\phi_w = \frac{1}{2}(\phi_P + \phi_W) &- \frac{c_x}{2}(\phi_P - \phi_W) - \frac{(1 - c_x^2)}{6}(\phi_P - 2\phi_W + \phi_{WW}) \\
&- \frac{c_y}{4}\left[(\phi_P - \phi_S) + (\phi_{NW} - \phi_W)\right] + \frac{c_y^2}{4}(\phi_{NW} - 2\phi_W + \phi_{SW}) \\
&+ \frac{c_x c_y}{4}(\phi_P - \phi_W - \phi_S + \phi_{SW})
\end{aligned} \tag{56}$$

with an analogous formula for ϕ_s. Note that the first three terms on the right of (56) represent the one-dimensional contribution, corresponding to the QUICKEST scheme (Leonard, 1979). The next term can be rewritten using the following identity

$$\begin{aligned}
\frac{(\phi_P - \phi_S) + (\phi_{NW} - \phi_W)}{4} \equiv \frac{(\phi_W - \phi_{SW})}{2} &+ \frac{(\phi_{NW} - 2\phi_W + \phi_{SW})}{4} \\
&+ \frac{(\phi_P - \phi_W - \phi_S + \phi_{SW})}{4}
\end{aligned} \tag{57}$$

in which case, the latter two terms on the right can be combined with the corresponding terms in (56), giving

$$\phi_w = \phi_{LIN} - \frac{c_x}{2}\,\mathrm{GRADNW} - \frac{(1 - c_x^2)}{6}\,\mathrm{CURVNW}$$

$$- \frac{c_y}{2}\,\mathrm{GRADTW}$$

$$- \frac{c_y}{4}\left[(1 - c_y)\,\mathrm{CURVTW} + (1 - c_x)\,\mathrm{TWISTW}\right] \tag{58}$$

where, as seen from (56), ϕ_{LIN} represents linear interpolation across the west face, GRADNW is the *normal-gradient* term, CURVNW represents the upwind-biased *normal-curvature* term (depending on the sign of c_x), GRADTW is the *transverse-gradient* term appearing earlier in lower-order formulae (depending on the signs of both c_x and c_y), CURVTW is the upwind-biased *transverse-curvature* term (depending on the sign of c_x), and TWISTW is a cross-difference or "*twist*" term (again depending on the signs of both velocity components at the face). Of course, the south-face value has an entirely analogous formula that can be easily derived by simple permutation of node-values.

Figure 12 shows the results of the standard test-problem using this uniformly third-order polynomial interpolation algorithm (UTOPIA). Clearly, there has been a significant improvement in performance, as compared with lower-order schemes. Isotropy is very good and peak resolution is reasonable, the only significant problem being the appearance of (relatively small) negative values in the out-skirts of the main profile region. In some cases, undershoots of this kind are merely an inconvenience. However, some transported variables may need to be kept strictly non-negative for both physical and (more importantly) stability reasons. In such cases, lack of positivity preservation could cause serious problems. UTOPIA's behaviour is relatively insensitive to stream-to-grid angle, as seen in Figure 13 ($\Theta = \tan^{-1} 0.5 \approx 26.565°$) and Figure 14 ($\Theta = 0°$). Perhaps surprisingly, the stability region is restricted to the diamond-shaped figure: $|c_x| + |c_y| < 1$, even though *exact* point-to-point transfer again occurs at $|c_x| = |c_y| = 1$ (evidently, these are isolated stable points).

For comparison, Figure 15 shows 45°-advection results using the (theoretically unstable) one-dimensional QUICKEST scheme in each coordinate direction separately; i.e., dropping the GRADT-, CURVT-, and TWIST-terms in (58). Such a two-dimensional advection scheme, together with standard second-order central differencing for diffusion, has been used for many years by Davis and Moore (1982, 1985) and co-workers. Once again, one sees considerable anisotropic distortion, although phase error is lower than that of second-order methods. For pure advection, this method is also theoretically *unstable*, unless the flow is exactly aligned with the grid. It is perhaps of interest to look at a "quasi-third-order" scheme in which face-values are given by the one-dimensional QUICKEST formulae, together with only the GRADT terms (i.e., omitting transverse curvature and twist terms, in order to effect some economisation). The 45°-advection results for this scheme are shown in Figure 16. Although much better than the uniformly second-order method, Figure 9 (in terms of phase error), or Davis and Moore's method (in terms of grid-orientation distortion), it is not immediately clear whether or not the savings incurred by algorithmic simplification might be more than offset by deterioration of the simulation. In other words, to achieve a

given accuracy it might be necessary to refine the grid using the ''quasi-third-order'' scheme to a point where it is actually more expensive, overall, than using UTOPIA on the original grid. This question can be answered by performing a series of grid-refinement studies and comparing the relative computational efficiency of each scheme, as done for steady-state flow, for example, by Leonard and Mokhtari (1990). A preliminary grid-refinement study of this kind is reported in Appendix 3, where it is shown that the uniformly third-order UTOPIA scheme is indeed significantly more efficient than the ''quasi-third-order'' scheme (which, in fact, is only second-order accurate). The stability region for the ''quasi-third-order'' method is the full square: $(1-|c_x|)(1-|c_y|) \geq 0$.

The advective-characteristic-tracking idea implied by (27) could, of course, be applied to uniformly higher-order interpolation methods. However, above third-order, algorithmic complexity increases rapidly, especially in terms of additional transverse and other mixed cross-difference terms. One strategy that appears to give quite good results without undue algorithmic complexity is to keep all third-order transverse and cross terms but expand the computational stencil for each advected face-value only in the *normal* direction. In other words, the one-dimensional contribution is expanded to higher order while keeping only third-order additional terms. For example, for the west face

$$\phi_w = \phi_w(\text{higher-order 1D}) - \frac{c_y}{2}\,\text{GRADTW}$$

$$- \frac{c_y}{4}\left[(1 - c_y)\,\text{CURVTW} + (1 - c_x)\,\text{TWISTW}\right] \tag{59}$$

This procedure has been explored by Leonard and Niknafs (1989), and appears to give good resolution and isotropy. Computational efficiency can be greatly enhanced by using an adaptive-stencil-expansion strategy; i.e., UTOPIA is used in smooth regions, whereas in regions containing large spatial gradients (or strong changes in gradient), the algorithm automatically extends the one-dimensional contribution to higher order on the basis of some non-smoothness monitor. This is highly cost-effective because the (more expensive) wider stencil is used only in isolated narrow (steep-gradient or high-curvature) regions involving a relatively small number of grid points.

The main problem with multidimensional, collocated polynomial methods (above first order) is that they are not inherently positivity preserving. This is also true, of course, in the one-dimensional case. For a given continuous profile, higher-order methods are better in this respect, but for near-discontinuities, any polynomial scheme will generate spurious unphysical overshoots and undershoots, which may feed back and totally disrupt the solution. This phenomenon has been demonstrated for one-dimensional scalar advection (up to ninth-order) by Leonard (1991). In one dimension, simple flux-limiting strategies can be devised to guarantee monotonicity preservation. The two-dimensional extension of these ideas appears to be much more difficult. Some flux limiters (such as one-dimensional TVD conditions applied coordinate-wise) appear to be *sufficient* for maintaining positivity under some (rather restrictive) conditions, but tend to generate strong grid-dependent distortion. Some progress in devising truly multidimensional (and less shape-distorting) flux limiters has, however, been made. This is discussed in the next section.

MULTIDIMENSIONAL FLUX-LIMITERS

Before tackling the multidimensional case, it is instructive to review the concepts of flux limiters for one-dimensional scalar advection. In this case, the model equation is

$$\frac{\partial \phi}{\partial t} + u \frac{\partial \phi}{\partial x} = 0 \tag{60}$$

where u is a (positive) constant. An explicit single forward time-step, control-volume update formula for this equation can be written in compass-point notation as

$$\phi_P^+ = \phi_P + c\,(\phi_w - \phi_e) \tag{61}$$

referring to west and east ''effective'' face-values (Leonard, 1991), where $c = u\,\Delta t/h$ is the Courant number. It is convenient to introduce a ''generic'' upwind-biased stencil. For example, near any given control-volume face (f), define upwind (U), downwind (D) and central (C) node values (on the basis of the sign of u) as shown in Figure 17(a). Now define a locally normalised variable

$$\tilde{\phi}(x) = \frac{\phi(x) - \phi_U^n}{\phi_D^n - \phi_U^n} \tag{62}$$

so that, in particular, $\tilde{\phi}_U^n = 0$ and $\tilde{\phi}_D^n = 1$. Figure 17(b) shows the corresponding $\tilde{\phi}_C^n$ node-value and the normalised face-value, $\tilde{\phi}_f$.

In one-dimensional flows, the main problem associated with maintaining monotonicity occurs when $\tilde{\phi}_P$ ($= \tilde{\phi}_C^n$) has a small (positive) value. If the interpolated $\tilde{\phi}_f$ value is too high, there will be too much flux advected out of the downwind face of the control-volume centred at C, and $\tilde{\phi}_P^+$ ($= \tilde{\phi}_C^{n+1}$) may be drawn down below zero, thereby destroying monotonicity. A different interpolation could avoid this problem by predicting a *smaller* $\tilde{\phi}_f$ value. This is shown schematically in Figure 18, where a parabolic interpolation (a) for the face-value, $\tilde{\phi}_f$, is compared with an exponential interpolation (b), for the same $\tilde{\phi}_C^n$ value. Over a time-step Δt, it is clear that the advective outflux predicted by case (a) would be *larger* than that of case (b). In order to derive the limiting conditions, assume first that $\tilde{\phi}_f$ lies between $\tilde{\phi}_C^n$ and 1

$$\tilde{\phi}_C^n \le \tilde{\phi}_f \le 1 \tag{63}$$

consistent with local interpolative monotonicity. Now consider (61) written in terms of normalised variables, and require the updated normalised value not to be negative

$$\tilde{\phi}_P^+ = \tilde{\phi}_P + c\,(\tilde{\phi}_w - \tilde{\phi}_e) \ge 0 \tag{64}$$

The situation is shown schematically in Figure 19. Referring to (63), written for the upstream (west) face, the worst-case (smallest) value for $\tilde{\phi}_w$ would be zero. From (64), this generates the condition

$$\tilde{\phi}_e \leq \frac{\tilde{\phi}_P}{c} \tag{65}$$

or, in general for any face, using the generic stencil of Figure 17,

$$\tilde{\phi}_f \leq \frac{\tilde{\phi}_C^n}{c} \quad \text{for} \quad 0 \leq \tilde{\phi}_C^n \leq 1 \tag{66}$$

One also needs to to consider suppression of overshoots when $\tilde{\phi}_P$ ($= \tilde{\phi}_C$ in Figure 18) is slightly less than 1, for example. In this case, conditions may need to be imposed on the upstream-face *influx* to keep it small enough so that the updated $\tilde{\phi}_P^+$ does not exceed 1. But (63) is sufficient to avoid this because the *largest* $\tilde{\phi}_w$-value is $\tilde{\phi}_P$, and this is also the *smallest* $\tilde{\phi}_e$-value, so that $\tilde{\phi}_P^+$ can never overshoot its adjacent downstream value (at very worst, it remains constant over a particular time-step). Thus (63) and (66) taken together are sufficient to guarantee monotonicity-preservation (i.e., suppression of both overshoots and undershoots) in the case of one-dimensional advection at constant velocity; and this has been borne out by numerical experiments (Leonard, 1991). Figure 20 summarises these "universal" limiter constraints for the monotonic range, $0 \leq \tilde{\phi}_C^n \leq 1$. In the non-monotonic range, several strategies are possible, one of the simplest being to set

$$\tilde{\phi}_f = \tilde{\phi}_C^n \quad \text{for} \quad \tilde{\phi}_C^n < 0 \quad \text{or} \quad \tilde{\phi}_C^n > 1 \tag{67}$$

this is also shown in Figure 20. The universal limiter is the basis for a number of higher-order, so-called "ULTIMATE", one-dimensional advection schemes developed by Leonard (1991). The acronym stands for "universal limiter for transient interpolation modelling of the advective transport equations."

The flux-limiter constraints used by total-variation-diminishing (TVD) schemes are rather more restrictive than those shown in Figure 20. First, it should be noted that TVD schemes use second-order time averaging. Referring to Figure 21, this means that the face-value is assumed to vary linearly with time, so that

$$\phi_f = \phi_f^n - \left(\frac{\partial \phi}{\partial x}\right) \frac{u\Delta t}{2} + O(\Delta t^2) \approx \phi_f^n - \left(\frac{\phi_f^n - \phi_C^n}{\Delta x/2}\right) \frac{u\Delta t}{2}$$

$$= (1 - c)\, \phi_f^n + c\, \phi_C^n \tag{68}$$

recalling that ϕ_f (without a superscript) denotes the time-average over Δt, whereas ϕ_f^n is the interpolated face-value at time-level n. As explained by Leonard and Mokhtari (1990), the TVD flux-limiter constraints summarised, for example, by Sweby (1984) can be written in terms of $\tilde{\phi}_f^n$ as

$$\tilde{\phi}_f^n \leq 2\tilde{\phi}_C^n \quad \text{for} \quad 0 \leq \tilde{\phi}_C^n \leq 0.5 \tag{69}$$

and

$$\tilde{\phi}_f^n \leq 1 \quad \text{for} \quad 0.5 \leq \tilde{\phi}_C^n \leq 1 \tag{70}$$

with

$$\tilde{\phi}_f^n \geq \tilde{\phi}_c^n \qquad \text{for} \quad 0 \leq \tilde{\phi}_c^n \leq 1 \tag{71}$$

and

$$\tilde{\phi}_f^n = \tilde{\phi}_c^n \qquad \text{for} \quad \tilde{\phi}_c^n < 0 \quad \text{or} \quad \tilde{\phi}_c^n > 1 \tag{72}$$

These are shown diagrammatically in Figure 22 (note that the vertical axis in this figure is $\tilde{\phi}_f^n$, not $\tilde{\phi}_f$). In order to compare with Figure 20 (where the ordinate is $\tilde{\phi}_f$, not $\tilde{\phi}_f^n$), it is necessary to rewrite the TVD constraints (69)-(72) in terms of $\tilde{\phi}_f$, using (68). This gives

$$\tilde{\phi}_f \leq (2 - c)\,\tilde{\phi}_c^n \qquad \text{for} \quad 0 \leq \tilde{\phi}_c^n \leq 0.5 \tag{73}$$

and

$$\tilde{\phi}_f \leq 1 + c\,(\tilde{\phi}_c^n - 1) \qquad \text{for} \quad 0.5 < \tilde{\phi}_c^n \leq 1 \tag{74}$$

with the other constraints remaining the same. The corresponding diagram is shown in Figure 23, where the slopes of the upper constraints are given by

$$S_1 = 2 - c \tag{75}$$

and

$$S_2 = c \tag{76}$$

These should be compared with $S_1 = 1/c$ and $S_2 = 0$ shown in Figure 20 for the (less-restrictive) universal limiter. The relationships between the upper-constraint slopes of ULTIMATE and TVD schemes are shown in Figure 24 as functions of Courant number, between $c = 0$ and 1.

In order to develop a two-dimensional positivity-preserving (PP) algorithm, one might try to use one-dimensional TVD or ULTIMATE fluxes in each coordinate direction separately (with c replaced by the local *normal* component Courant number at each face). For example, the TVD (CLAM) scheme of van Leer (1974) can be described in terms of $\tilde{\phi}_f^n$ by

$$\tilde{\phi}_f^n = 2\tilde{\phi}_c^n - (\tilde{\phi}_c^n)^2 \qquad \text{for} \quad 0 \leq \tilde{\phi}_c^n \leq 1 \tag{77}$$

with $\tilde{\phi}_f^n = \tilde{\phi}_c^n$ elsewhere. This is shown in Figure 25. Note how the slope of the parabolic curve is tangent to the TVD constraints as $\tilde{\phi}_c^n \rightarrow 0_+$ and 1_-. Also note that $\tilde{\phi}_f^n = 0.75$ when $\tilde{\phi}_c^n = 0.5$, making this a second-order scheme in "smooth" regions ($\tilde{\phi}_c^n \rightarrow 0.5$). Figure 26 shows the 2D results (for $c_x = c_y = 0.25$ and $\Theta = 45°$) of using the 1D CLAM scheme coordinate-wise. Although the scheme is evidently positivity preserving, there is considerable grid-orientation-dependent distortion, with cross-wind elongation and a tendency towards flattening along grid lines, producing a diamond-shaped distortion of the initially circular profile. The cross-wind elongation is primarily due to the lack of GRADT-terms. If these terms are included (before limiting), cross-wind elongation is reduced but the profile still tends to "square-up" along grid-lines. Also, as shown theoretically below, there are rather severe PP restrictions on the allowable component Courant-number ranges.

Figure 27 shows results of using the *one-dimensional* third-order ULTIMATE QUICKEST scheme in each coordinate direction separately. In addition to cross-wind elongation (due primarily to the lack of cross-terms), it can be seen that this scheme is not

positivity preserving. There is no point in trying to improve isotropy because, as is shown theoretically below, using the one-dimensional universal limiter coordinate-wise cannot guarantee positivity. The following analysis is based on a suggestion by Bull (personal communication, 1990). Referring to Figure 28, consider a *normalised* monotonic "front" passing through a control volume so that post-frontal node-values are essentially zero, with pre-frontal values close to unity. At the time indicated, the positions of the leading-edge (LE) and trailing-edge (TE) of the front are such that the normalised node-value at the control-volume center is a small positive value, $\tilde{\phi}_P = \tilde{\epsilon}$. This is the analogue of the one-dimensional case shown in Figure 18. If outfluxes significantly exceed influxes, the central node-value at the next time-level could be drawn down to negative values, thus destroying positivity. To avoid this, the following condition would be required for the updated variable, $\tilde{\phi}_P^+$,

$$\tilde{\phi}_P^+ = \tilde{\epsilon} + c_x(\tilde{\phi}_w - \tilde{\phi}_e) + c_y(\tilde{\phi}_s - \tilde{\phi}_n) \geq 0 \tag{78}$$

For the situation illustrated (c_x, $c_y > 0$), the worst-case condition corresponds to $\tilde{\phi}_w$ and $\tilde{\phi}_s$ both being as small as possible ($= 0$) and $\tilde{\phi}_e$ and $\tilde{\phi}_n$ both as large as possible. According to Figure 20 (with $\tilde{\phi}_C^n = \tilde{\epsilon}$), using the individual *normal* component Courant numbers, the universal-limiter constraints imply

$$\tilde{\phi}_e(\text{large}) = \frac{\tilde{\epsilon}}{c_x} \tag{79}$$

and

$$\tilde{\phi}_n(\text{large}) = \frac{\tilde{\epsilon}}{c_y} \tag{80}$$

Thus (78) becomes

$$\tilde{\phi}_P^+ = \tilde{\epsilon} + c_x\left(0 - \frac{\tilde{\epsilon}}{c_x}\right) + c_y\left(0 - \frac{\tilde{\epsilon}}{c_y}\right) = -\tilde{\epsilon} \tag{81}$$

thereby violating the PP inequality. This means that the one-dimensional universal limiter used coordinate-wise cannot guarantee multidimensional positivity preservation.

On the other hand, consider the TVD constraints of Figure 23. In this case (with $\tilde{\phi}_w$ and $\tilde{\phi}_s$ still both equal to zero),

$$\tilde{\phi}_e(\text{large}) = (2 - c_x)\,\tilde{\epsilon} \tag{82}$$

and

$$\tilde{\phi}_n(\text{large}) = (2 - c_y)\,\tilde{\epsilon} \tag{83}$$

Hence, the updated central node-value now becomes

$$\begin{aligned} \tilde{\phi}_P^+ &= \tilde{\epsilon} + c_x\left[0 - (2 - c_x)\,\tilde{\epsilon}\right] + c_y\left[0 - (2 - c_y)\,\tilde{\epsilon}\right] \\ &= \tilde{\epsilon}\left[1 - c_x(2 - c_x) - c_y(2 - c_y)\right] \end{aligned} \tag{84}$$

This expression is non-negative only if

$$(c_x - 1)^2 + (c_y - 1)^2 \geq 1 \quad \text{for} \quad 0 \leq (c_x, c_y) \leq 1 \tag{85}$$

This represents a rather severe restriction on the allowable ranges of the component Courant numbers, as seen by the circular arcs in Figure 29. In particular, for $\Theta = 45°$, c_x and c_y must both be less than $(1 - \sqrt{1/2}) \approx 0.293$. Even more restrictive conditions are required in three dimensions (see Appendix 4).

First Multidimensional Limiter

In order to devise less restrictive positivity-preserving conditions, return attention again to Figure 28 and Equation (78). Assume that the slope S_1 in Figure 20 *is to be found* in order to satisfy (78). Also assume that (63) still holds, so there can be no (normalised) overshoots (because, at least for a solenoidal velocity field, total influx cannot then exceed total outflux, for the same reasons as in the one-dimensional case) and, therefore, the only condition that needs to be considered is the avoidance of undershoots. This means that, instead of (79) and (80), the worst-case outflow face-values are written in terms of the (as yet unknown) slopes, S_1^x and S_1^y, as

$$\tilde{\phi}_e(\text{large}) = S_1^x \, \tilde{\epsilon} \tag{86}$$

and

$$\tilde{\phi}_n(\text{large}) = S_1^y \, \tilde{\epsilon} \tag{87}$$

where (for the moment) it is assumed that S_1^x and S_1^y may be different but related by symmetry according to

$$S_1^x = S_1(c_x, c_y) \tag{88}$$

and

$$S_1^y = S_1(c_y, c_x) \tag{89}$$

Substitution into (78) gives

$$\tilde{\phi}_P^+ = \tilde{\epsilon} + c_x(0 - S_1^x \, \tilde{\epsilon}) + c_y(0 - S_1^y \, \tilde{\epsilon}) \geq 0 \tag{90}$$

resulting in the condition

$$1 - c_x S_1^x - c_y S_1^y \geq 0 \tag{91}$$

The most general solution of this inequality would require

$$S_1^x \leq \frac{f(c_x, c_y)}{c_x f(c_x, c_y) + c_y f(c_y, c_x)} = S_1(c_x, c_y) \tag{92}$$

and

$$S_1^y \leq S_1(c_y, c_x) \tag{93}$$

where f is a (not necessarily symmetrical) function of c_x and c_y, to be chosen. Note that if $c_y = 0$ and $f(0, c_x)$ is finite, then

$$S_1(c_x, 0) = \frac{1}{c_x} \tag{94}$$

consistent with the one-dimensional formula. Also, at $\Theta = 45°$,

$$S_1(c, c) = \frac{1}{2c} \tag{95}$$

This means, in particular, that at $c_x = c_y = 0.5$,

$$S_1(0.5, 0.5) = 1 \tag{96}$$

regardless of the form of f. If f is in fact symmetrical, then it cancels in (92) leaving

$$S_1(c_x, c_y) = S_1^y = S_1 = \frac{1}{|c_x| + |c_y|} \tag{97}$$

where absolute values have been included to generalise to cases involving negative velocity components. This is the least restrictive (i.e., largest) symmetric form satisfying (91). Less restrictive non-symmetrical forms might be found by specifying the functional form of f. However, this strategy will not be pursued here. Of course, S_1 cannot be less than one, as this would violate the left-hand inequality of (63). Figure 30 shows contour lines of S_1 within the allowable region ($S_1 \geq 1$). Results of using this two-dimensional limiter in conjunction with the QUICKEST scheme in each coordinate direction are shown in Figure 31 for $\Theta = 45°$. The simulation is positivity preserving, but again there is considerable cross-wind elongation due to lack of cross-terms, together with steepening in the flow direction and concomitant flattening of the peak.

One could, of course, restore the cross-terms missing from the QUICKEST scheme and apply the limiter, (97), to the fully-third order UTOPIA scheme. Results are shown in Figure 32 for $c_x = c_y = 0.25$. The diamond-shaped distortion is quite disappointing; as advection proceeds further, the profile tends to square-up along grid lines. Apparently, the limiter represented by (97) is overly restrictive. For example, (97) shows that the slope of the limiter becomes 1 along the boundary lines

$$|c_x| + |c_y| = 1 \tag{98}$$

seen in Figure 30. This means that, for Courant numbers in ranges near these boundaries, the simulation is approaching the highly artificially diffusive and *anisotropic* first-order scheme given by (19), with results similar to those shown in Figure 4.

Second Multidimensional Limiter

Some progress toward better isotropy can be made by incorporating the transverse-gradient terms *after* the limiting step. Assume that ϕ_f^0 is a higher-order face-value not including GRADT terms. For example, the west-face UTOPIA ϕ_f^0 would be given by (58), omitting the GRADTW term; i.e.,

$$\phi_w^0 = \phi_{LIN} - \frac{c_x}{2}\,\mathrm{GRADNW} - \frac{(1 - c_x^2)}{6}\,\mathrm{CURVNW}$$

$$- \frac{c_y}{4}\left[(1 - c_y)\,\mathrm{CURVTW} + (1 - c_x)\,\mathrm{TWISTW}\right] \tag{99}$$

Now assume that this temporary face value, written in normalised form as $\tilde{\phi}_f^0$, is constrained, near $\tilde{\phi}_C^n \to 0_+$, by

$$\tilde{\phi}_C^n \le \tilde{\phi}_f^0 \le \tilde{\phi}_{\mathrm{REF1}} = S_1\,\tilde{\phi}_C^n \tag{100}$$

where S_1 remains to be found in order to satisfy PP conditions. Working in terms of *un*normalised variables, the right-hand reference value can be written

$$\phi_{\mathrm{REF1}} = \phi_U + S_1(\phi_C - \phi_U) \tag{101}$$

using the generic-stencil notation of Figure 17.

Referring to Figure 11, the update algorithm in *un*normalised variables can be written (for constant velocity) as

$$\phi_P^+ = \phi_P + c_x(\phi_w - \phi_e) + c_y(\phi_s - \phi_n) \tag{102}$$

Now write the actual face-values as the algebraic sum of the temporary values and the appropriate transverse-gradient terms. For c_x and c_y both positive, these take the form

$$\phi_w = \phi_w^0 - \frac{c_y}{2}(\phi_W - \phi_{SW}) \tag{103}$$

$$\phi_e = \phi_e^0 - \frac{c_y}{2}(\phi_P - \phi_S) \tag{104}$$

$$\phi_s = \phi_s^0 - \frac{c_x}{2}(\phi_S - \phi_{SW}) \tag{105}$$

$$\phi_n = \phi_n^0 - \frac{c_x}{2}(\phi_P - \phi_W) \tag{106}$$

Substitution into (102) gives

$$\phi_P^+ = \phi_P + c_x c_y(\phi_P - \phi_W - \phi_S + \phi_{SW}) + c_x(\phi_w^0 - \phi_e^0) + c_y(\phi_s^0 - \phi_n^0) \tag{107}$$

Consider first, non-negative node-values increasing in the flow direction, with ϕ_P quite small. The aim is to avoid the updated ϕ_P^+ becoming negative. Once again consider worst-case small influxes and large outfluxes. If ϕ_W and ϕ_S are small (but non-negative), then the left-hand inequality of (100) gives the worst-case inflow values as

$$\phi_w^0(\text{small}) = \phi_W \tag{108}$$

and

$$\phi_s^0(\text{small}) = \phi_S \tag{109}$$

The largest outflow values need to be constrained by the slope S_1. In terms of unnormalised variables, referring to (101),

$$\phi_e^0(\text{large}) = \phi_W + S_1^x(\phi_P - \phi_W) \tag{110}$$

and

$$\phi_n^0(\text{large}) = \phi_S + S_1^y(\phi_P - \phi_S) \tag{111}$$

where again (for the moment) S_1^x and S_1^y are assumed to be possibly different but symmetrically related. Substitution of (108)-(111) into (107) gives

$$\begin{aligned}\phi_P^+ = {} & \phi_P\left[1 + c_x c_y - c_x S_1^x - c_y S_1^y\right] + c_x c_y \phi_{SW} \\ & + c_x(S_1^x - c_y)\phi_W + c_y(S_1^y - c_x)\phi_S\end{aligned} \tag{112}$$

and this is required to be non-negative for arbitrary, non-negative ϕ_P, ϕ_{SW}, ϕ_W, and ϕ_S. Thus the coefficients of each of these node-values must all be non-negative. An upper bound on S_1^x and S_1^y is obtained by setting the coefficient of ϕ_P to zero, the corresponding conditions for ϕ_W and ϕ_S providing lower bounds. The upper bound is chosen, as this yields the *least* restrictive limiter. This implies

$$S_1^x \leq \frac{(1 + c_x c_y) f(c_x, c_y)}{c_x f(c_x, c_y) + c_y f(c_y, c_x)} = S_1(c_x, c_y) \tag{113}$$

and, by symmetry,

$$S_1^y \leq S_1(c_y, c_x) \tag{114}$$

where, again, f is some (in general not necessarily symmetrical) function to be specified. As before, this S_1 is consistent with the one-dimensional case; but at 45°

$$S_1(c, c) = \frac{1 + c^2}{2c} \tag{115}$$

which is now always greater than (or equal to) 1.

Once again, if f is a symmetric function of c_x and c_y, the (only) symmetrical form of S_1 becomes

$$S_1^x = S_1^y \leq S_1 = \frac{(1 + c_x c_y)}{(c_x + c_y)} \tag{116}$$

From (112) this gives

$$\phi_P^+ \geq c_x c_y \phi_{SW} + \frac{c_x(1 - c_y^2)}{(c_x + c_y)} \phi_W + \frac{c_y(1 - c_x^2)}{(c_y + c_x)} \phi_S \tag{117}$$

And since, for stability, $|c_x|$ and $|c_y|$ are both less than or equal to 1, the updated node-value is indeed non-negative. Unsymmetrical forms could perhaps lead to somewhat less restrictive conditions, but these are not pursued here.

However, it turns out that (116) is not sufficient for giving PP results in general. One must also consider (positive) node-values *decreasing* in the flow direction, as well. This will require restrictions on $\tilde{\phi}_f^0$ near $\tilde{\phi}_C^n \to 1_-$. Specifically, assume that, in normalised-variable notation,

$$\tilde{\phi}_C^n \leq \tilde{\phi}_f^0 \leq \tilde{\phi}_{\text{REF2}} = 1 + S_2(\tilde{\phi}_C^n - 1) \tag{118}$$

near $\tilde{\phi}_C^n \to 1_-$. In terms of *un*normalised generic variables, (118) can be rewritten as

$$\phi_C^n \geq \phi_f^0 \geq \phi_{\text{REF2}} = \phi_D + S_2(\phi_C - \phi_D) \tag{119}$$

using the notation of Figure 17. The inequality reversal is due to the *negative* normalising denominator in this case. In a decreasing region, worst-case conditions (tending to make the control-volume central node-value negative) imply

$$\phi_e^0(\text{large}) = \phi_P \tag{120}$$

and

$$\phi_n^0(\text{large}) = \phi_P \tag{121}$$

as well. The smallest allowable inflow face-values, according to (119), are

$$\phi_w^0(\text{small}) = \phi_P + S_2^x(\phi_W - \phi_P) \tag{122}$$

and

$$\phi_s^0(\text{small}) = \phi_P + S_2^y(\phi_S - \phi_P) \tag{123}$$

where

$$S_2^x = S_2(c_x, c_y) \tag{124}$$

and, by symmetry,

$$S_2^y = S_2(c_y, c_x) \tag{125}$$

Substitution of (120)-(123) into (107) gives

$$\phi_P^+ = \phi_P(1 + c_x c_y - c_x S_2^x - c_y S_2^y) + c_x c_y \phi_{SW}$$

$$+ c_x(S_2^x - c_y)\phi_W + c_y(S_2^y - c_x)\phi_S \tag{126}$$

Choosing the *smallest* (and therefore least restrictive) S_2's as

$$S_2^x = c_y \tag{127}$$

and

$$S_2^y = c_x \tag{128}$$

eliminates the ϕ_W and ϕ_S terms and results in

$$\phi_P^+ = \phi_P(1 - c_x c_y) + c_x c_y \phi_{SW} \tag{129}$$

Since this represents a weighted linear interpolation between the two (nonnegative) node-values, ϕ_{SW} and ϕ_P, the result (for $|c_x c_y| \leq 1$) is also nonnegative, approaching ϕ_P for small $|c_x c_y|$ and equalling ϕ_{SW} for $|c_x c_y| \equiv 1$ (consistent with exact point-to-point transfer across the grid diagonal).

The two-dimensional PP limiter restrictions on $\tilde{\phi}_f^0$ are summarised in Figure 33, where, for a *constant* velocity and corresponding component Courant numbers, c_x and c_y, allowing for positive or negative velocities,

$$S_1 = \frac{1 + |c_x c_y|}{|c_x| + |c_y|} \tag{130}$$

and

$$S_2^x = |c_y|, \qquad S_2^y = |c_x| \tag{131}$$

Contour plots of (130) are shown in Figure 34. As seen from the contours in Figure 34, there is a rather large region where S_1 is only slightly greater than 1 (e.g., see the large region between the contours $S_1 = 1.25$ and $S_1 = 1$); however, this is still less restrictive than the first two-dimensional limiter, given by (97).

Figures 35 through 39 show results of using the limiter given by (130) and (131) in combination with the UTOPIA scheme (i.e., with transverse-gradient terms restored after limiting but all other terms included beforehand). In Figure 35, $c_x = c_y = 0.25$ ($\Theta = 45°$); in Figure 36, $c_x = 0.25$ and $c_y = c_x/2$ ($\Theta \approx 26.565°$); in Figure 37, $c_x = 0.25$ and $c_y = c_x/3$ ($\Theta \approx 18.435°$); and in Figure 38, $c_x = 0.5$, $c_y = 0$ ($\Theta = 0°$). These results are seen to be generally much better than those using the first two-dimensional limiter given by (97). However, at $c_x = c_y = 0.5$ ($\Theta = 45°$) shown in Figure 39, there appears to be somewhat more distortion. In this case, the limiter slopes are $S_1 = 1.25$ and $S_2 = 0.5$, representing rather restrictive constraints. At larger Courant number values the simulation becomes noticeably more diffusive.

Extension to Variable Velocity

The two-dimensional flux-limiters developed so far have been based on a uniform advecting velocity field at an angle to the grid. Clearly, this is too restrictive to be of use in practical calculations involving variable velocity fields. However, the same principles can be generalised to variable *solenoidal* velocity fields satisfying the constant-density continuity equation

$$\nabla \cdot \mathbf{V} = 0 \tag{132}$$

For simplicity, only the first two-dimensional limiter will be extended here. The extension of the second limiter is more complicated and will be taken up in a future report.

Consider the update equation for variable velocity using conventional compass-point notation at each face

$$\phi_P^+ = \phi_P + c_{xw}\phi_w - c_{xe}\phi_e + c_{ys}\phi_s - c_{yn}\phi_n \tag{133}$$

where, by continuity

$$c_{xw} - c_{xe} + c_{ys} - c_{yn} = 0 \tag{134}$$

Four separate cases need to be considered:

(i) Two inflows on adjacent faces together with outflows on the other faces. This is represented by all c's being positive, for example.

(ii) One inflow and three outflows.

(iii) Three inflows and one outflow.

(iv) Inflows on opposite faces and outflows on the remaining faces.

These are sketched in Figure 40. In Case (i), Figure 40(a), the worst-case update becomes, in terms of unnormalised variables,

$$\phi_P^+ = \phi_P + c_{xw}\phi_W - c_{xe}\left[\phi_W + S_1(\phi_P - \phi_W)\right] + c_{ys}\phi_S - c_{yn}\left[\phi_S + S_1(\phi_P - \phi_S)\right] \tag{135}$$

or

$$\phi_P^+ = \phi_P\left[1 - S_1(c_{xe} + c_{yn})\right] + \phi_W\left[c_{xw} + c_{xe}(S_1 - 1)\right] + \phi_S\left[c_{ys} + c_{yn}(S_1 - 1)\right] \tag{136}$$

Choosing

$$S_1 = \frac{1}{c_{xe} + c_{yn}} \tag{137}$$

gives positivity-preserving results. This is the appropriate limiter slope for use on *both* the east and north faces—i.e., on the *outflow* faces for the CV cell under consideration. For the conditions of Case (i), but for other combinations of signs of the Courant number components, (137) can be immediately generalised, for two outflowing faces, to

$$S_1 = \frac{1}{|c_n^{\text{out}}|_1 + |c_n^{\text{out}}|_2} \tag{138}$$

using an obvious notation.

For Case (ii) shown in Figure 40(b), the worst-case update becomes

$$\phi_P^+ = \phi_P + c_{xw}\phi_W - c_{xe}\left[\phi_W + S_1(\phi_P - \phi_W)\right]$$
$$- |c_{ys}|\left[\phi_N + S_1(\phi_P - \phi_N)\right] - c_{yn}\left[\phi_S + S_1(\phi_P - \phi_S)\right] \tag{139}$$

or

$$\phi_P^+ = \phi_P\left[1 - S_1(c_{xe} + c_{yn} + |c_{ys}|)\right] + \phi_W\left[c_{xw} + c_{xe}(S_1 - 1)\right]$$
$$+ \phi_S\left[c_{yn}(S_1 - 1)\right] + \phi_N\left[|c_{ys}|(S_1 - 1)\right] \tag{140}$$

In this case, noting that c_{xe} and c_{yn} are both positive,

$$S_1 = \frac{1}{c_{xe} + c_{yn} + |c_{ys}|} \quad \left(= \frac{1}{c_{xw}} \right) \tag{141}$$

is the appropriate limiter slope for *each* of the *three outflow* face-values. Again, this can be generalised for three outflowing faces as

$$S_1 = \frac{1}{|c_n^{\text{out}}|_1 + |c_n^{\text{out}}|_2 + |c_n^{\text{out}}|_3} \tag{142}$$

It is not difficult to see that similar formulae would apply in Cases (iii) and (iv).

In summary, the limiter slope for any face is computed as follows:

(i) Identify the control-volume cell for which the face in question is an *outflow* face.

(ii) Take the S_1 slope for that face as

$$S_1 = \frac{1}{\sum |c_n^{\text{out}}|} \tag{143}$$

where the sum is over *all outflow* faces for the identified CV cell (including the face in question).

A similar strategy can easily be devised for three-dimensional flow in an obvious way. This type of flux-limiter has been tested for scalar advection in 2D and 3D solenoidal velocity fields. As expected, results are positivity-preserving to machine accuracy, even when discontinuities are present in the initial conditions. Details will be given in a subsequent report.

CONCLUSION

Advection is a key dynamical process in many areas of fluid dynamics. As computer power has increased and the spatial resolution of CFD codes has improved, so the need for more accurate numerical advection schemes has increased in significance. This is because the higher spatial resolution allows (in principle) the representation of sharper gradients and changes in gradient. More detailed resolution of advective transport means that less empiricism has to be used in modelling important fluid-dynamic processes. Unfortunately, as is well known, traditional advection methods, such as the space-time-centred leap-frog scheme, do not perform well under highly advective conditions, often exhibiting large regions of spurious numerical oscillations. Such behaviour may be manifested in CFD simulations as, for example, negative values of density concentrations, or other unphysical phenomena. Numerically dispersive advection schemes of this type may even generate a kind of ''numerical turbulence'' that, in turn, can lead to the erroneous prediction of anomalous mixing processes. These features may interact with the physical parameterizations within the models and lead to significant degradation of numerical simulations and forecasts.

Two aspects of accurate advective modelling have been addressed in the present report. The first concerns the problem of anisotropic distortion—i.e., the dependence of the solution on grid orientation. Methods based on using one-dimensional formulae in each coordinate direction separately show strong anisotropic distortion at non-zero flow-to-grid angles. The introduction of transverse-gradient cross-terms into the advective fluxes greatly alleviates this problem in second-order methods. However, the multidimensional, uniformly second-order method (the generalised conservative Lax-Wendroff scheme) is still too numerically dispersive for use as the basis for a good CFD advection code. Fortunately, the techniques used to derive this method generalise to higher order. As in the case of one-dimensional advection, the multidimensional, uniformly third-order, polynomial interpolation algorithm (UTOPIA) possesses several desirable properties. The conservative, control-volume formulation is relatively straight-forward algorithmically, isotropy appears to be excellent, and phase error is low. Because of the flux-based, conservative formulation, ''mass'' is conserved (to machine accuracy). The only drawback (as with all collocated polynomial schemes above first order) is that it is not inherently positivity-preserving.

In order to produce a multidimensional, positivity-preserving advection scheme, one might consider using well-known one-dimensional TVD flux-limiters in each coordinate direction. However, this approach has been shown here to have two shortcomings: the allowable Courant-number range is very limited, and results are again highly grid-dependent, showing a strong ''squaring-off'' distortion along grid-lines. The anisotropy appears to be due partly to the use of one-dimensional limiter formulae (which are inherently grid-orientation dependent) and partly to the fact that TVD limiters, in general, are overly restrictive, tending to add (coordinate-wise) artificial diffusion locally, in order to suppress potential oscillations.

One of the main focuses of the current work has been to generalise the less-restrictive universal limiter concepts originally developed for one-dimensional flows by Leonard (1991). The one-dimensional universal limiter applied coordinate-wise in two dimensions has been shown theoretically not to preserve positivity. However, the analysis used in deriving this result also suggests two different multidimensional generalisations that are symmetric with

respect to x- and y-component Courant numbers (and are consistent with the one-dimensional case). Unfortunately, the first multidimensional limiter, (97), reintroduces considerable anisotropic distortion. The second multidimensional limiter, given by (130) and (131), is based on adding the transverse-gradient terms *after* the limiting process. In this way, reasonably good isotropy is maintained when applied to an inherently isotropic advection scheme such as UTOPIA. Fortunately, both the advection scheme itself and the limiter constraints can be generalised in a straight-forward manner to three dimensions (see Appendix 1 and Appendix 5, respectively). Appendix 2 also outlines the inclusion of physical diffusion terms to a consistent order, and a simple upwinding strategy designed to avoid IF statements is sketched in Appendix 6.

The multidimensional third-order advection scheme and the generalised limiter constraints were initially derived on the basis of uni-directional constant-velocity linear scalar advection. Similar principles have been applied in the case of spatially varying *solenoidal* velocity fields using the first multidimensional limiter. Generalisation of the second multidimensional limiter to variable velocity fields is more complicated, and will be discussed elsewhere. The main aim of this research project has been to advance the state of the art of advection modelling beyond standard techniques (generally involving gross anisotropic distortion and potentially disastrous numerical dispersion). And, to the extent that this has been achieved, highly advective modelling should be enhanced. This will become apparent when the current strategy has been implemented in production codes and applied to real fluid-dynamic processes.

ACKNOWLEDGMENTS

Parts of this research were carried out while the first author was a Visiting Research Scientist at the Atmospheric Processes Research Division of the U.K. Meteorological Office in Bracknell. The authors are indebted to Mark Bull, formerly of the Meteorological Office, who pointed out the two-dimensional TVD Courant-number restrictions and the non-positivity-preserving results of using the universal limiter one-dimensionally in a multi-dimensional problem.

APPENDIX 1

THREE-DIMENSIONAL FORMULAE

In three dimensions, the computational molecule for third-order upwinding consists of the twenty nodes shown in Figure A.1.1, where the notation refers to the conventional compass-points (N, S, E, W) together with top (T) and bottom (B) levels. Note the upwind bias, assuming that the Courant number components, c_x, c_y, and c_z are all positive. Taking local coordinates centered at P, the ϕ-value at time-level n can be written

$$\begin{aligned}\phi^n(\xi,\eta,\zeta) \;=\; & C_1 + C_2\,\xi + C_3\,\xi^2 + C_4\,\xi^3 \\ & + C_5\,\eta + C_6\,\eta^2 + C_7\,\eta^3 \\ & + C_8\,\zeta + C_9\,\zeta^2 + C_{10}\,\zeta^3 \\ & + C_{11}\,\xi\,\eta + C_{12}\,\xi\,\eta^2 + C_{13}\,\xi^2\,\eta \\ & + C_{14}\,\eta\,\zeta + C_{15}\,\eta\,\zeta^2 + C_{16}\,\eta^2\,\zeta \\ & + C_{17}\,\zeta\,\xi + C_{18}\,\zeta\,\xi^2 + C_{19}\,\zeta^2\,\xi + C_{20}\,\xi\,\eta\,\zeta \qquad \text{(A.1.1)}\end{aligned}$$

This should be compared with (44); note the obvious similarity in structure, but also note the appearance of the triple-product C_{20}-term. Because of the similarity with the two-dimensional case, evaluation of the coefficients by collocation follows a predictable pattern:

$$C_1 = \phi_P \qquad \text{(A.1.2)}$$

$$C_2 = \frac{\phi_E - \phi_W}{2\Delta x} - \frac{\phi_E - 3\phi_P + 3\phi_W - \phi_{WW}}{6\Delta x} \qquad \text{(A.1.3)}$$

$$C_3 = \frac{\phi_E - 2\phi_P + \phi_W}{2\Delta x^2} \qquad \text{(A.1.4)}$$

$$C_4 = \frac{\phi_E - 3\phi_P + 3\phi_W - \phi_{WW}}{6\Delta x^3} \qquad \text{(A.1.5)}$$

$$C_5 = \frac{\phi_N - \phi_S}{2\Delta y} - \frac{\phi_N - 3\phi_P + 3\phi_S - \phi_{SS}}{6\Delta y} \qquad \text{(A.1.6)}$$

$$C_6 = \frac{\phi_N - 2\phi_P + \phi_S}{2\Delta y^2} \qquad \text{(A.1.7)}$$

$$C_7 = \frac{\phi_N - 3\phi_P + 3\phi_S - \phi_{SS}}{6\Delta y^3} \tag{A.1.8}$$

$$C_8 = \frac{\phi_T - \phi_B}{2\Delta z} - \frac{\phi_T - 3\phi_P + 3\phi_B - \phi_{BB}}{6\Delta z} \tag{A.1.9}$$

$$C_9 = \frac{\phi_T - 2\phi_P + \phi_B}{2\Delta z^2} \tag{A.1.10}$$

$$C_{10} = \frac{\phi_T - 3\phi_P + 3\phi_B - \phi_{BB}}{6\Delta z^3} \tag{A.1.11}$$

$$C_{11} = \frac{(\phi_E - \phi_P) - (\phi_{SE} - \phi_S) + (\phi_N - \phi_{NW}) - (\phi_P - \phi_W)}{2\Delta x\,\Delta y} \tag{A.1.12}$$

$$C_{12} = \frac{(\phi_N - \phi_{NW}) - 2(\phi_P - \phi_W) + (\phi_S - \phi_{SW})}{2\Delta x\,\Delta y^2} \tag{A.1.13}$$

$$C_{13} = \frac{(\phi_E - \phi_{SE}) - 2(\phi_P - \phi_S) + (\phi_W - \phi_{SW})}{2\Delta x^2\,\Delta y} \tag{A.1.14}$$

$$C_{14} = \frac{(\phi_E - \phi_P) - (\phi_{BE} - \phi_B) + (\phi_T - \phi_{TW}) - (\phi_P - \phi_W)}{2\Delta y\,\Delta z} \tag{A.1.15}$$

$$C_{15} = \frac{(\phi_T - \phi_{TW}) - 2(\phi_P - \phi_W) + (\phi_B - \phi_{BW})}{2\Delta y\,\Delta z^2} \tag{A.1.16}$$

$$C_{16} = \frac{(\phi_N - \phi_{BN}) - 2(\phi_P - \phi_B) + (\phi_S - \phi_{BS})}{2\Delta y^2\,\Delta z} \tag{A.1.17}$$

$$C_{17} = \frac{(\phi_E - \phi_P) - (\phi_{BS} - \phi_B) + (\phi_T - \phi_{TW}) - (\phi_P - \phi_W)}{2\Delta z\,\Delta x} \tag{A.1.18}$$

$$C_{18} = \frac{(\phi_E - \phi_{BE}) - 2(\phi_P - \phi_B) + (\phi_W - \phi_{BW})}{2\Delta z\,\Delta x^2} \tag{A.1.19}$$

$$C_{19} = \frac{(\phi_T - \phi_{TW}) - 2(\phi_P - \phi_W) + (\phi_B - \phi_{BW})}{2\Delta z^2 \Delta x} \tag{A.1.20}$$

$$C_{20} = \frac{(\phi_P - \phi_W - \phi_S + \phi_{SW}) - (\phi_B - \phi_{BW} - \phi_{BS} + \phi_{BSW})}{\Delta x \Delta y \Delta z} \tag{A.1.21}$$

In terms of a three-dimensional velocity, $\mathbf{V} = (u, v, w)$, the advective back-tracking formula can be written

$$\phi_P^+ = \phi^n(-u\Delta t, -v\Delta t, -w\Delta t) \tag{A.1.22}$$

When this and the above C-values are substituted into (A.1.1), the resulting formula can be rearranged into a flux-based, conservative, control-volume, single time-step, explicit update algorithm of the form

$$\begin{aligned}\phi_P^+ = {} & \phi_P + \mathrm{FLUXW}(i, j, k) + \mathrm{FLUXS}(i, j, k) + \mathrm{FLUXB}(i, j, k) \\ & - \mathrm{FLUXW}(i+1, j, k) - \mathrm{FLUXS}(i, j+1, k) - \mathrm{FLUXB}(i, j, k+1)\end{aligned} \tag{A.1.23}$$

where, for example,

$$\mathrm{FLUXW}(i, j, k) = c_x \phi_w \tag{A.1.24}$$

and so on. By analogy with the two-dimensional case it is not difficult to show that the advected west face-value, for example, is given by

$$\begin{aligned}\phi_w = {} & \phi_{LIN} - \frac{c_x}{2}\mathrm{GRADNW} - \frac{(1 - c_x^2)}{6}\mathrm{CURVNW} \\ & - \frac{c_y}{2}\mathrm{GRDTYW} - \frac{c_z}{2}\mathrm{GRDTZW} \\ & - \frac{c_y}{4}\left[(1 - c_y)\,\mathrm{CRVTYW} + (1 - c_x)\,\mathrm{TWSTYW}\right] \\ & - \frac{c_z}{4}\left[(1 - c_z)\,\mathrm{CRVTZW} + (1 - c_x)\,\mathrm{TWSTZW}\right] \\ & + \frac{c_y c_z}{3}\mathrm{TWSYZW}\end{aligned} \tag{A.1.25}$$

Where ϕ_{LIN} is the linear interpolation across the west face

$$\phi_{LIN} = \frac{1}{2}(\phi_P + \phi_W) \tag{A.1.26}$$

the normal gradient is given by

$$\text{GRADNW} = \phi_P - \phi_W \tag{A.1.27}$$

and the upwind-biased normal curvature is

$$\text{CURVNW} = \phi_P - 2\phi_W + \phi_{WW} \tag{A.1.28}$$

just as in the one-dimensional formula. The two (two-dimensional) upwind-biased transverse-gradient terms are given by

$$\text{GRDTYW} = \phi_W - \phi_{SW} \tag{A.1.29}$$

and

$$\text{GRDTZW} = \phi_W - \phi_{BW} \tag{A.1.30}$$

The transverse-curvature and (x, y)- and (x, z)-twist terms also have the same (upwind-biased) form as their two-dimensional counterparts

$$\text{CRVTYW} = \phi_{NW} - 2\phi_W + \phi_{SW} \tag{A.1.31}$$

$$\text{CRVTZW} = \phi_{TW} - 2\phi_W + \phi_{BW} \tag{A.1.32}$$

$$\text{TWSTYW} = \phi_P - \phi_S - \phi_W + \phi_{SW} \tag{A.1.33}$$

and

$$\text{TWSTZW} = \phi_P - \phi_B - \phi_W + \phi_{BW} \tag{A.1.34}$$

Finally, the last term in (A.1.25) is a peculiarly three-dimensional term representing an upwind-biased (y, z)-twist contribution

$$\text{TWSYZW} = \phi_W - \phi_{SW} - \phi_{BW} + \phi_{BSW} \tag{A.1.35}$$

Figure A.1.2 shows the ten node-values involved in computing ϕ_w (for c_x, c_y, $c_z > 0$). The other face-values, ϕ_s and ϕ_b, can be obtained by using a straight-forward permutation process. However, this is not necessary, because a ''generic'' stencil can be used for any control-volume face, determined by the signs of the individual local Courant number components. This is outlined for the two-dimensional case in Appendix 6. The three-dimensional extension is straight-forward.

APPENDIX 2

INCLUSION OF DIFFUSION TERMS

Consider the advection-diffusion equation written in conservation form as

$$\frac{\partial \phi}{\partial t} + \nabla \cdot (\mathbf{V}\phi) = \nabla \cdot (D \nabla \phi) \tag{A.2.1}$$

A numerical update formula can be written in the form of (A.1.23) provided each flux contains both advective and diffusive contributions. For example, the west-face flux is given by

$$\mathrm{FLUXW}(i, j, k) = c_{xw}\,\phi_w - \alpha_{xw}\left(\frac{\partial \phi}{\partial x}\right)_w \Delta x \tag{A.2.2}$$

introducing the diffusion parameter, α_{xw}, defined by

$$\alpha_{xw} = \frac{D_w\,\Delta t}{\Delta x^2} \tag{A.2.3}$$

Similarly for the other faces. The task now is to estimate the face-value and face-gradient appearing in (A.2.2). At third order (and above) one needs to consider the effect of diffusion in estimating ϕ_w and, conversely, the effect of advection in estimating $(\partial\phi/\partial x)_w$.

In order to assess these effects, consider the constant-coefficient one-dimensional advection-diffusion model equation

$$\frac{\partial \phi}{\partial t} = -u\frac{\partial \phi}{\partial x} + D\frac{\partial^2 \phi}{\partial x^2} \tag{A.2.4}$$

Now formally integrate this equation in time, from 0 to τ. At the west face, for example, this gives

$$\phi_w(\tau) = \phi_w(0) - \int_0^\tau \left(u\frac{\partial \phi}{\partial x}\right)_w d\tau + \int_0^\tau \left(D\frac{\partial^2 \phi}{\partial x^2}\right)_w d\tau \tag{A.2.5}$$

The first integral on the right represents the variation of ϕ_w with time due to purely advective effects (obtained by setting $D = 0$); the second integral represents the diffusive contribution. The latter term is estimated simply as

$$\int_0^\tau \left(D\frac{\partial^2 \phi}{\partial x^2}\right)_w d\tau \approx \int_0^\tau \left(D\frac{\partial^2 \phi}{\partial x^2}\right)_w^n d\tau = \left(D\frac{\partial^2 \phi}{\partial x^2}\right)_w^n \tau \tag{A.2.6}$$

Averaging $\phi_w(\tau)$ over $\tau = 0 \rightarrow \Delta t$, then leads to

$$\phi_w = \phi_w(\mathrm{adv}) + \left(D\frac{\partial^2 \phi}{\partial x^2}\right)_w^n \frac{\Delta t}{2} \tag{A.2.7}$$

where the first term is the purely advective contribution to the time-average and the second term an estimate of the diffusive contribution. Equation (A.2.7) can be rewritten as

$$\phi_w = \phi_w(\text{adv}) + \frac{\alpha_{xw}}{2} \text{CURV}_w^n \tag{A.2.8}$$

where CURV_w^n is an appropriate second-difference. By equating CURV_w^n with the upwind-biased (normal) curvature term, the one-dimensional third-order time-averaged face-value can be written

$$\phi_w = \phi_{LIN} - \frac{c_{xw}}{2} \text{GRADL} - \left[\frac{(1 - c_{xw}^2)}{6} - \frac{\alpha_{xw}}{2}\right] \text{CURVL} \tag{A.2.9}$$

Clearly, (A.2.7) can be generalised to two and three dimensions by writing for the west face, say,

$$\phi_w = \phi_w(\text{adv}) + (D\nabla^2\phi)_w^n \frac{\Delta t^2}{2} \tag{A.2.10}$$

This generalises (A.1.25) to the following form

$$\begin{aligned}
\phi_w = \phi_{LIN} &- \frac{c_{xw}}{2} \text{GRADNW} - \left[\frac{(1 - c_{xw}^2)}{6} - \frac{\alpha_{xw}}{2}\right] \text{CURVNW} \\
&- \frac{c_{yw}}{2} \text{GRDTYW} - \frac{c_{zw}}{2} \text{GRDTZW} \\
&- \left[\frac{c_{yw}}{4}(1 - c_{yw}) - \frac{\alpha_{xw}}{2}\right] \text{CRVTYW} - \frac{c_{yw}}{4}(1 - c_{xw}) \text{TWSTYW} \\
&- \left[\frac{c_{zw}}{4}(1 - c_{zw}) - \frac{\alpha_{xw}}{2}\right] \text{CRVTZW} - \frac{c_{zw}}{4}(1 - c_{xw}) \text{TWSTZW} \\
&+ \frac{c_{yw} c_{zw}}{3} \text{TWSYZW}
\end{aligned} \tag{A.2.11}$$

For estimating the time-averaged normal gradient across a given face, refer first to the one-dimensional case sketched in Figure A.2.1. In time Δt, the curved profile shown is advected to the right; thus, the face-gradient is continuously changing with time according to the linear relationship

$$\left(\frac{\partial \phi}{\partial x}\right)_w^\tau = \left(\frac{\partial \phi}{\partial x}\right)_w^0 - \left(\frac{\partial^2 \phi}{\partial x^2}\right)_w^n u_w \tau + O(\tau^2) \tag{A.2.12}$$

The time-averaged gradient over Δt is therefore

$$\left(\frac{\partial \phi}{\partial x}\right)_w = \left(\frac{\partial \phi}{\partial x}\right)_w^0 - \left(\frac{\partial^2 \phi}{\partial x^2}\right)_w^n \frac{u_w \Delta \tau}{2} + O(\Delta t^2) \tag{A.2.13}$$

This can be rewritten as

$$\left(\frac{\partial \phi}{\partial x}\right)_w \Delta x \approx \text{GRADW} - \frac{c_w}{2}\text{CURV}_w^n \tag{A.2.14}$$

where CURV_w^n is an appropriate second-difference in the vicinity of the west face. Once again it is convenient to use the upwind-biased curvature term, CURVW. In the one-dimensional case the approximate gradient is therefore given by

$$\left(\frac{\partial \phi}{\partial x}\right)_w \Delta x = \text{GRADW} - \frac{c_w}{2}\text{CURVW} \tag{A.2.15}$$

In two and three dimensions, the normal gradient will vary with time due to twist terms, as well. It is not hard to generalise (A.2.15) for the west face, for example, to give

$$\left(\frac{\partial \phi}{\partial x}\right)_w \Delta x = \text{GRADNW} - \frac{c_{xw}}{2}\text{CURVNW} - \frac{c_{yw}}{2}\text{TWSTYW} - \frac{c_{zw}}{2}\text{TWSTZW} \tag{A.2.16}$$

The total west-face flux is given by substituting (A.2.11) and (A.2.16) into (A.2.2).

For a model constant-coefficient form of the governing advection-diffusion equation

$$\frac{\partial \phi}{\partial t} + \mathbf{V}\cdot\nabla\phi = D\nabla^2\phi \tag{A.2.17}$$

it is possible to derive an exact three-dimensional complex amplitude ratio, $\mathbf{G}_{\text{exact}}$. Use of (A.2.11) and (A.2.16) and corresponding formulas for the other faces then produces an algorithm whose $\mathbf{G}$-expansion agrees with that of $\mathbf{G}_{\text{exact}}$ through all third-order terms in the wave-number components. Specifically, consider a three-dimensional plane wave of the form

$$\phi = \mathbf{A}(t)\exp(\iota\,\mathbf{k}\cdot\mathbf{x}) \tag{A.2.18}$$

where the vector wave-number is given by

$$\mathbf{k} = k_x\hat{\mathbf{i}} + k_y\hat{\mathbf{j}} + k_z\hat{\mathbf{k}} \tag{A.2.19}$$

Substitution into (A.2.17) then gives

$$\phi = A(0)\exp[-\mathbf{k}\cdot\mathbf{k}Dt]\exp[\iota\,\mathbf{k}\cdot(\mathbf{x}-\mathbf{V}t)] \tag{A.2.20}$$

Assume constant grid spacing, $\Delta x = \Delta y = \Delta z = h$, and define

$$\alpha = \frac{D\Delta t}{h^2} \tag{A.2.21}$$

$$\theta = \mathbf{k}h \tag{A.2.22}$$

and

$$\mathbf{c} = \frac{\mathbf{V}\Delta t}{h} \tag{A.2.23}$$

Then the exact three-dimensional complex amplitude ratio is given by

$$\mathbf{G}_{\text{exact}} = \exp(-\alpha\,\theta^2)\,\exp[-\iota(\mathbf{c}\cdot\boldsymbol{\theta})] \tag{A.2.24}$$

where $\theta^2 = \boldsymbol{\theta}\cdot\boldsymbol{\theta}$. Expanding real and imaginary parts gives

$$\begin{aligned}
\mathbf{G}_{\text{exact}} = {} & 1 - \left[\alpha\,\theta^2 + \frac{1}{2}(\mathbf{c}\cdot\boldsymbol{\theta})^2\right] \\
& + \left[\frac{\alpha^2}{2}\theta^4 + \frac{\alpha}{2}\theta^2(\mathbf{c}\cdot\boldsymbol{\theta})^2 + \frac{1}{24}(\mathbf{c}\cdot\boldsymbol{\theta})^4\right] + \ldots \\
& - \iota \left\{ \begin{array}{l} \mathbf{c}\cdot\boldsymbol{\theta} - \left[\alpha\,\theta^2(\mathbf{c}\cdot\boldsymbol{\theta}) + \frac{1}{6}(\mathbf{c}\cdot\boldsymbol{\theta})^3\right] \\ + \left[\frac{\alpha^2}{2}\theta^4(\mathbf{c}\cdot\boldsymbol{\theta}) + \frac{\alpha}{6}\theta^2(\mathbf{c}\cdot\boldsymbol{\theta})^3 + \frac{1}{120}(\mathbf{c}\cdot\boldsymbol{\theta})^5\right] \\ + \ldots \end{array} \right\}
\end{aligned} \tag{A.2.25}$$

A von Neumann analysis of the generalised UTOPIA scheme, incorporating the effects of diffusion on advection and *vice versa*, as described above, leads to

$$\begin{aligned}
\mathbf{G}_{\text{UTOPIA}} = {} & 1 - \left[\alpha\,\theta^2 + \frac{1}{2}(\mathbf{c}\cdot\boldsymbol{\theta})^2\right] + \ldots \\
& - \iota \left\{ \mathbf{c}\cdot\boldsymbol{\theta} - \left[\alpha\,\theta^2(\mathbf{c}\cdot\boldsymbol{\theta}) + \frac{1}{6}(\mathbf{c}\cdot\boldsymbol{\theta})^3\right] + \ldots \right\}
\end{aligned} \tag{A.2.26}$$

thus matching $\mathbf{G}_{\text{exact}}$ through all third-order terms in the $\boldsymbol{\theta}$-components.

APPENDIX 3

GRID-REFINEMENT STUDIES

Some preliminary grid-refinement studies have been made for some of the schemes discussed in this report. All of the tests are for an angle of $\Theta = \tan^{-1}(1/2) \approx 26.525°$, using Courant numbers $c_x = 0.5$ and $c_y = 0.25$. The number of time-steps, N, is chosen so that the exact solution would move 2 units in the x-direction and 1 unit in the y-direction. This means that

$$N = \frac{2}{c_x h} \tag{A.3.1}$$

In addition to the base case of $h^{-1} = 31$, the grid is refined to $h^{-1} = 61$, 121, and 241.

At each grid point, the final-time error is computed by subtracting the theoretically exact value from the computed value

$$\epsilon_{i,j} = \phi_{i,j} - \phi_{ex}(x_i, y_j) \tag{A.3.2}$$

An L_1 global error diagnostic is also computed from

$$L_1 = h^2 \sum_{i=1}^{1/h} \sum_{j=1}^{1/h} |\epsilon_{i,j}| \tag{A.3.3}$$

The following tables show the total number of time-steps, N, the grid-refinement, h^{-1}, the minimum nodal ϕ-value, the maximum nodal ϕ-value, the maximum (signed) error, the L_1 error, the CPU time (on a CRAY-YMP, to the nearest second), and the computation time relative to the 2D Lax-Wendroff scheme. The convergence rates for the maximum error and the L_1 error are taken to the nearest integer.

Table A.3.1 2D Lax-Wendroff

N	h^{-1}	ϕ_{min}	ϕ_{max}	ϵ_{max}	L_1	CPU time	Rel. time
124	31	-1.13×10^{-1}	0.822	3.75×10^{-1}	3.09×10^{-2}	3	1
244	61	-1.43×10^{-2}	0.965	1.46×10^{-1}	8.34×10^{-3}	24	1
484	121	-3.16×10^{-6}	0.995	3.85×10^{-2}	2.13×10^{-3}	188	1
964	241	$+2.16 \times 10^{-11}$	0.9994	9.53×10^{-3}	5.35×10^{-4}	1485	1
CONVERGENCE RATE				$O(h^2)$	$O(h^2)$		

Table A.3.2 1D QUICKEST with GRADT terms

N	h^{-1}	ϕ_{min}	ϕ_{max}	ϵ_{max}	L_1	CPU time	Rel. time
124	31	-3.24×10^{-2}	0.844	-1.66×10^{-1}	1.26×10^{-2}	4	1.208
244	61	-2.19×10^{-4}	0.973	-3.91×10^{-2}	3.20×10^{-3}	29	1.208
484	121	-5.17×10^{-8}	0.997	-8.50×10^{-3}	7.96×10^{-4}	227	1.208
964	241	-1.43×10^{-11}	0.9996	-2.02×10^{-3}	1.99×10^{-4}	1794	1.208
CONVERGENCE RATE				$O(h^2)$	$O(h^2)$		

Table A.3.3 UTOPIA

N	h^{-1}	ϕ_{min}	ϕ_{max}	ϵ_{max}	L_1	CPU time	Rel. time
124	31	-5.93×10^{-3}	0.872	-1.28×10^{-1}	6.47×10^{-3}	4	1.333
244	61	-1.02×10^{-5}	0.977	-2.29×10^{-2}	9.95×10^{-4}	31	1.333
484	121	$+6.01 \times 10^{-11}$	0.997	-3.07×10^{-3}	1.30×10^{-4}	249	1.333
964	241	$+1.67 \times 10^{-11}$	0.9996	-3.86×10^{-4}	1.60×10^{-5}	1980	1.333
CONVERGENCE RATE				$O(h^3)$	$O(h^3)$		

Table A.3.4 UTOPIA with first 2D limiter

N	h^{-1}	ϕ_{min}	ϕ_{max}	ϵ_{max}	L_1	CPU time	Rel. time
124	31	7.80×10^{-8}	0.716	3.95×10^{-1}	3.15×10^{-2}	5	1.505
244	61	2.48×10^{-7}	0.888	4.23×10^{-1}	2.14×10^{-2}	36	1.505
484	121	3.76×10^{-8}	0.943	2.95×10^{-1}	1.31×10^{-2}	283	1.505
964	241	1.75×10^{-9}	0.956	1.65×10^{-1}	7.40×10^{-3}	2235	1.505
CONVERGENCE RATE				$O(h)$	$O(h)$		

Table A.3.5 UTOPIA with second 2D limiter

N	h^{-1}	ϕ_{min}	ϕ_{max}	ϵ_{max}	L_1	CPU time	Rel. time
124	31	3.00×10^{-9}	0.711	-2.89×10^{-1}	1.05×10^{-2}	5	1.623
244	61	1.44×10^{-10}	0.886	-1.15×10^{-1}	3.27×10^{-3}	39	1.623
484	121	5.42×10^{-11}	0.957	$+5.72 \times 10^{-2}$	8.26×10^{-4}	305	1.623
964	241	3.35×10^{-11}	0.984	$+2.59 \times 10^{-2}$	2.06×10^{-4}	2410	1.623
CONVERGENCE RATE				$O(h)$	$O(h^2)$		

APPENDIX 4

THREE DIMENSIONAL TVD CONSTRAINTS

In three dimensions, TVD flux-limiters can be used component-wise but, as in the two-dimensional case, there will be restrictions on the component Courant numbers mandated by positivity preservation. The three-dimensional update equation corresponding to (84) is

$$\tilde{\phi}_P^+ = \tilde{\epsilon} + c_x[0 - (2 - c_x)\,\tilde{\epsilon}] + c_y[0 - (2 - c_y)\,\tilde{\epsilon}] + c_z[0 - (2 - c_z)\,\tilde{\epsilon}] \geq 0 \tag{A.4.1}$$

This is equivalent to

$$(c_x - 1)^2 + (c_y - 1)^2 + (c_z - 1)^2 \geq 2 \tag{A.4.2}$$

for $(c_x, c_y, c_z \leq 1)$. The boundary of the positivity-preserving region is thus a portion of a sphere of radius $\sqrt{2}$. For $c_x = c_y = c_z = c$, this means that

$$c \leq 1 - \sqrt{2/3} \approx 0.184 \tag{A.4.3}$$

compared with $c \leq 1 - \sqrt{1/2} \approx 0.293$ in the two-dimensional case. Clearly, (A.4.2) represents a rather severe restriction on the allowable time step.

APPENDIX 5

THREE-DIMENSIONAL LIMITER

The three-dimensional generalisation of (130) and (131) can be derived in a straight-forward manner. For finding the slope S_1, refer to Figure A.1.1. By analogy with (112), the update algorithm can be written

$$\begin{aligned}\phi_P^+ = {} & \phi_P\left[1 + c_x c_y + c_y c_z + c_z c_x - (c_x + c_y + c_z)\,S_1\right] \\ & + c_x(S_1 - c_y - c_z)\,\phi_W + c_y(S_1 - c_z - c_x)\,\phi_S + c_z(S_1 - c_x - c_y)\,\phi_B \\ & + c_x c_y\,\phi_{SW} + c_y c_z\,\phi_B + c_z c_x\,\phi_{BW}\end{aligned} \tag{A.5.1}$$

and this is required to be nonnegative. The ϕ_P-term can be eliminated by choosing

$$S_1 = \frac{(1 + c_x c_y + c_y c_z + c_z c_x)}{(c_x + c_y + c_z)} \tag{A.5.2}$$

Note that this is consistent with the two-dimensional formula ($c_z = 0$) and the one-dimensional case ($c_y = c_z = 0$). The coefficient of ϕ_W, for example, then becomes

$$\frac{c_x(1 - c_y c_z - c_y^2 - c_z^2)}{(c_x + c_y + c_z)} \tag{A.5.3}$$

with similar formulas for the coefficients of ϕ_S and ϕ_B obtained by permutation. These coefficients become negative in a rather significant portion of the (c_x, c_y, c_z) space for which $S_1 \geq 1$, thus further restricting the PP region.

The analogue of (126) becomes

$$\begin{aligned}\phi_P^+ = {} & \phi_P(1 + c_x c_y + c_y c_z + c_z c_x - c_x S_2^x - c_y S_2^y - c_z S_2^z) \\ & + c_x(S_2^x - c_y - c_z)\phi_W + c_y(S_2^y - c_z - c_x)\phi_S + c_z(S_2^z - c_x - c_y)\phi_B \\ & + c_x c_y \phi_{SW} + c_y c_z \phi_{BS} + c_z c_x \phi_{BW}\end{aligned} \tag{A.5.4}$$

Eliminating ϕ_W, ϕ_S, and ϕ_B gives

$$S_2^x = c_y + c_z \tag{A.5.5}$$

$$S_2^y = c_z + c_x \tag{A.5.6}$$

$$S_2^z = c_x + c_y \tag{A.5.7}$$

resulting in

$$\begin{aligned}\phi_P^+ = {} & \phi_P(1 - c_x c_y - c_y c_z - c_z c_x) \\ & + c_x c_y \phi_{SW} + c_y c_z \phi_{BS} + c_z c_x \phi_{BW}\end{aligned} \tag{A.5.8}$$

representing a nonnegative weighting, provided

$$c_x c_y + c_y c_z + c_z c_x \leq 1 \tag{A.5.9}$$

From the S_2 formulae it can be seen that, unfortunately, one of the S_2's becomes unity whenever any two Courant number components are simultaneously equal to 0.5. For some applications this may be too restrictive. Further generalisations, re-introducing the non-symmetrical f function in order to find less restrictive limiter constraints, are currently being explored.

APPENDIX 6

UPWINDING STRATEGY WITHOUT IF STATEMENTS

Clearly, in order to take account of all combinations of signs of the Courant number components at any given face, the upwinding strategy could become quite complicated. Using IF statements to branch to a different formula for each combination is conceptually straight-forward but computationally very expensive. Figure A.6.1 shows the four combinations for a given face in the two-dimensional case, using a generic stencil notation representing upwind (U), downwind (D), central (C), etc., similar to Figure 17(a) for the one-dimensional case. Assume that the face in question is the left face of a particular control volume centred at node (I, J). The following upwinding strategy avoids IF statements, relying instead on the signs of the Courant number components at the face, and the FORTRAN nearest-integer function, NINT.

Figure A.6.2 shows the labelling of node-values for the west face of a control volume (I, J) according to the signs of c_{xw} and c_{yw}. Note that any of the cases in Figure A.6.1 can be viewed in the form of Figure A.6.2 (imagine a case in A.6.1 drawn on a sheet of transparent film; by rotating and/or turning over the sheet, the configuration can always be made to conform to that in A.6.2). Using the nearest-integer function, NINT, the node labels can be described in terms of the signs of c_{xw} and c_{yw} as follows:

$$\text{IWU} = \text{I} - \text{NINT}\left[0.5 + \text{SIGN}(1.5,\ c_{xw})\right] \tag{A.6.1}$$

$$\text{IWC} = \text{I} - \text{NINT}\left[0.5 + \text{SIGN}(0.5,\ c_{xw})\right] \tag{A.6.2}$$

$$\text{IWD} = \text{I} - \text{NINT}\left[0.5 - \text{SIGN}(0.5,\ c_{xw})\right] \tag{A.6.3}$$

$$\text{JWU} = \text{J} - \text{NINT}\left[\text{SIGN}(1.0,\ c_{yw})\right] \tag{A.6.4}$$

and

$$\text{JWD} = \text{J} + \text{NINT}\left[\text{SIGN}(1.0,\ c_{yw})\right] \tag{A.6.5}$$

The six node-values of the generic third-order west-face stencil are given by

$$\phi^{w}_{CD} = \phi(\text{IWC, JWD}) \tag{A.6.6}$$

$$\phi^{w}_{U} = \phi(\text{IWU, J}) \tag{A.6.7}$$

$$\phi^{w}_{C} = \phi(\text{IWC, J}) \tag{A.6.8}$$

$$\phi_D^w = \phi(\text{IWD, J}) \tag{A.6.9}$$

$$\phi_{CU}^w = \phi(\text{IWC, JWU}) \tag{A.6.10}$$

and

$$\phi_{DU}^w = \phi(\text{IWD, JWU}) \tag{A.6.11}$$

The UTOPIA west face-value corresponding to (58) is then given by

$$\phi_w = \phi_{LIN} - \frac{|c_{xw}|}{2}\text{GRADNW} - \frac{(1 - c_{xw}^2)}{6}\text{CURVNW} - \frac{|c_{yw}|}{2}\text{GRADTW}$$

$$- \frac{|c_{yw}|}{4}\left[(1 - |c_{yw}|)\,\text{CURVTW} - (1 - |c_{xw}|)\,\text{TWISTW}\right] \tag{A.6.12}$$

where

$$\phi_{LIN} = \frac{1}{2}\left(\phi_D^w + \phi_C^w\right) \tag{A.6.13}$$

$$\text{GRADNL} = \phi_D^w - \phi_C^w \tag{A.6.14}$$

$$\text{CURVNL} = \phi_D^w - 2\phi_C^w + \phi_U^w \tag{A.6.15}$$

$$\text{GRADTL} = \phi_C^w - \phi_{CU}^w \tag{A.6.16}$$

$$\text{CURVTL} = \phi_{CD}^w - 2\phi_C^w + \phi_{CU}^w \tag{A.6.17}$$

and

$$\text{TWISTL} = \phi_D^w - \phi_C^w - \phi_{DU}^w + \phi_{CU}^w \tag{A.6.18}$$

Higher-order formulas corresponding to (59) can be designed in an obvious way. Note particularly the use of the absolute-values of the Courant number components in (A.6.12). A similar procedure is easily constructed for the other (south) face (in two dimensions). And it should be clear that the extension to three dimensions follows the same strategy for each of the three face-values involved for any given control volume.

REFERENCES

1. Bull, J.M.: Recent Developments in Numerical Methods for the Advection Equation and their Application to Boundary Layer Modelling. Met O (P) Turbulence and Diffusion Note No. 195, 1990.

2. Davis, R.W.; and Moore, E.F.: A Numerical Study of Vortex Shedding from Rectangles. *J. Fluid Mech.*, vol. **116**, no. 3, 1982, pp. 475-506.

3. Davis, R.W.; and Moore, E.F.: A Numerical Study of Vortex merging in Mixing Layers. *Phys. Fluids*, vol. **28**, no. 6, 1985, pp. 1626-1635.

4. Lax, P.D.; and Wendroff, B.: Systems of Conservation Laws. *Commun. Pure Appl. Math.*, vol. **13**, no. 2, 1960, pp. 217-237.

5. Leonard, B.P.: A Stable and Accurate Convective Modeling Procedure Based on Quadratic Upstream Interpolation. *Comput. Methods Appl. Mech. Eng.*, vol. **19**, June 1979, pp. 59-98.

6. Leonard, B.P.: The ULTIMATE Conservative Difference Scheme Applied to Unsteady One-Dimensional Advection. *Comput. Methods Appl. Mech. Eng.*, vol. **88**, June 1991, pp. 17-74.

7. Leonard, B.P.; and Mokhtari, S.: Beyond First-Order Upwinding: The ULTRA-SHARP Alternative for Nonoscillatory Steady-State Simulation of Convection. *Int. J. Numer. Methods Eng.*, vol. **30**, no. 2, 1990, pp. 141-154.

8. Leonard, B.P.; and Niknafs, H.S.: Cost-Effective Accurate Coarse-Grid Method for Highly Convective Multidimensional Unsteady Flow. Computational Fluid Dynamics Symposium on Aeropropulsion, NASA CP-3078, 1991, pp. 227-240.

9. Sweby, P.K.: High Resolution Schemes Using Flux Limiters for Hyperbolic Conservation Laws. *SIAM J. Numer. Anal.*, vol. **21**, no. 5, 1984, pp. 995-1011.

10. Van Leer, B.: Towards the Ultimate Conservative Difference Scheme. II. Monotonicity and Conservation Combined in a Second-Order Scheme. *J. Comput. Phys.*, vol. **14**, no. 4, 1974, pp. 361-370.

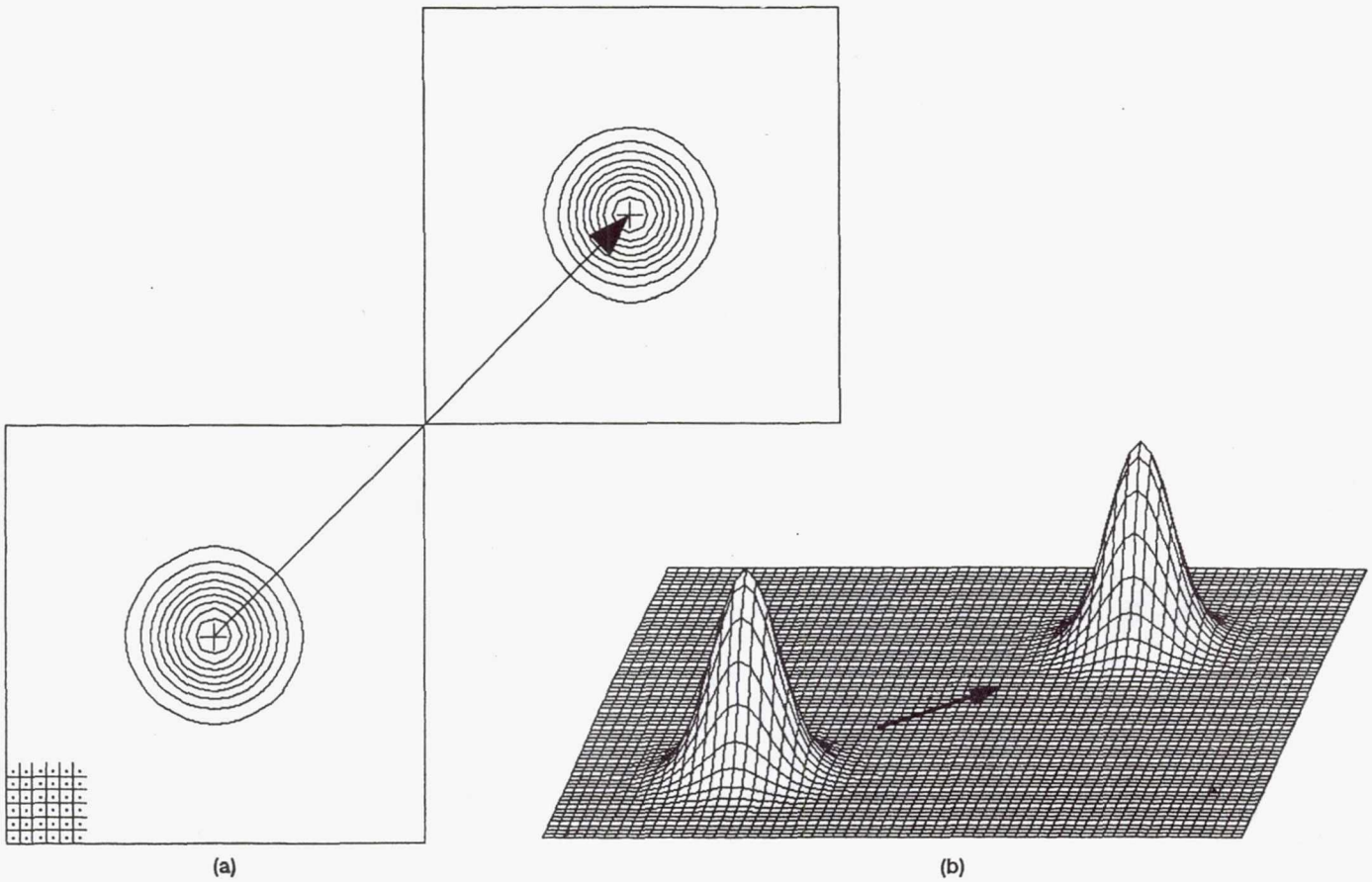

Figure 1.—Schematic of exact solution for $\theta = 45°$. The small cross (+) indicates the geometric centre of the domain at grid point (16, 16). Note that boundaries correspond to control-volume cell faces. Periodic boundary conditions imply: $\phi(32, j) \equiv \phi(1, j)$, $\phi(i, 32) \equiv \phi(i, 1)$, etc. Positive "density" contours in this and all subsequent contour-plots are shown in increments of 0.1.

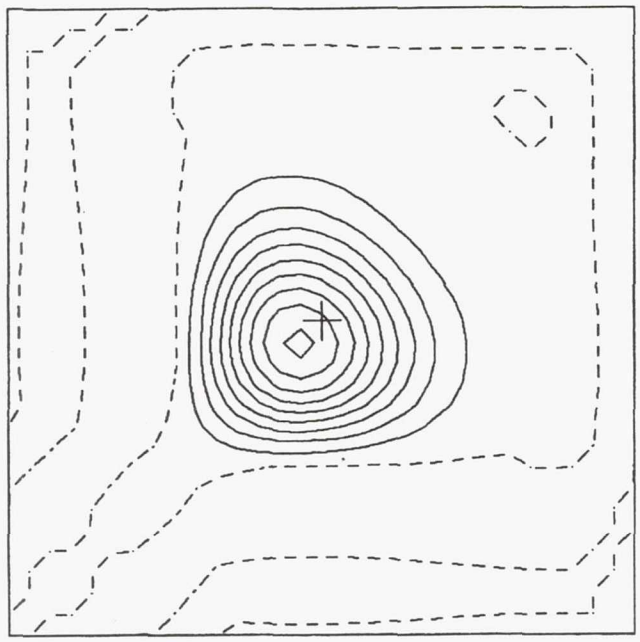

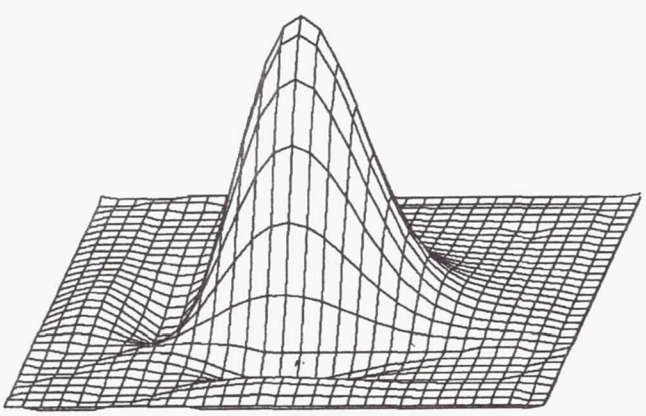

Figure 2.—Results for the leap-frog scheme for $\theta = 45°$; $c_x = c_y = 0.25$; $N = 1/c_x h = 124$, $\Delta t = \sqrt{2}/124$. Negative contours shown dashed ($\phi = -0.001, -0.05$). $\phi_{max} = 0.928$, $\phi_{min} = -0.091$.

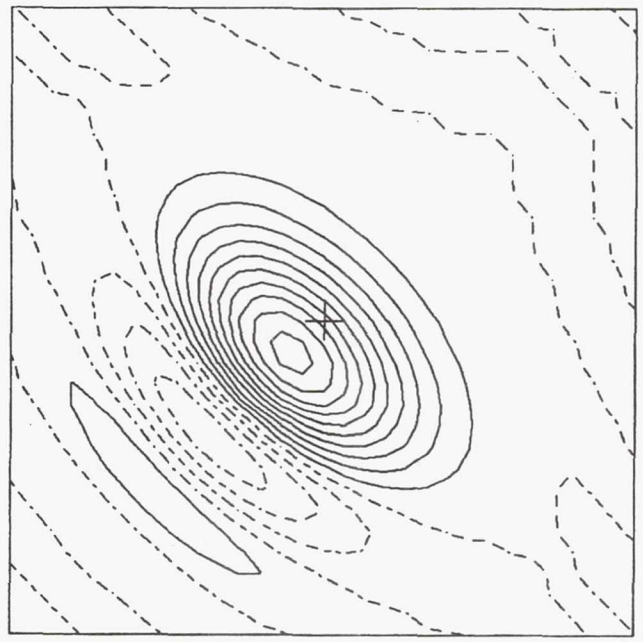

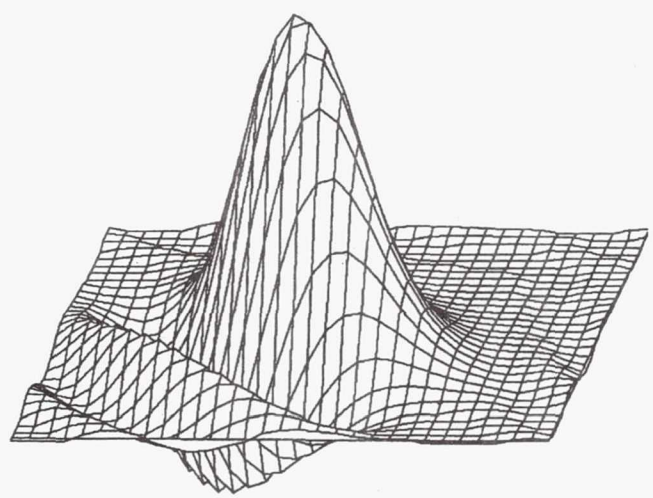

Figure 3.—Results for the one-dimensional Lax-Wendroff scheme used coordinate-wise for $\theta = 45°$; $c_x = c_y = 0.25$; $N = 124$, $\Delta t = \sqrt{2}/124$. Negative contours are: $\phi = -0.0001, -0.1, -0.2, -0.3$. Note the phase lag, slight overshoot ($\phi_{max} = 1.040$), and large undershoots ($\phi_{min} = -0.366$).

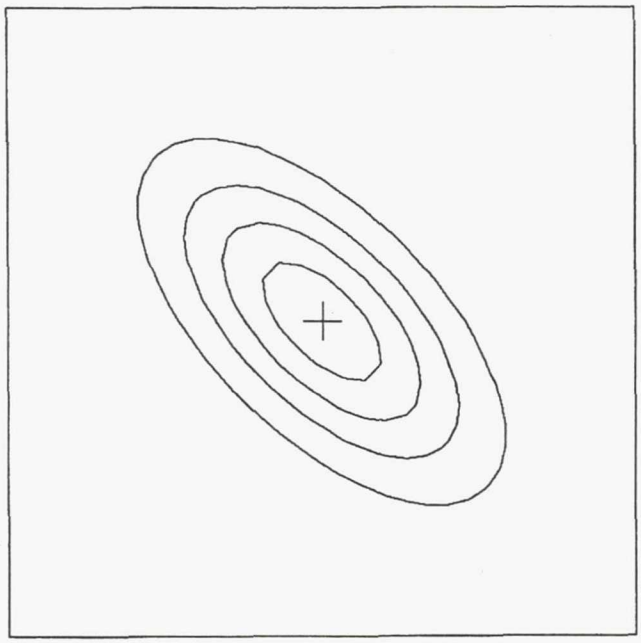

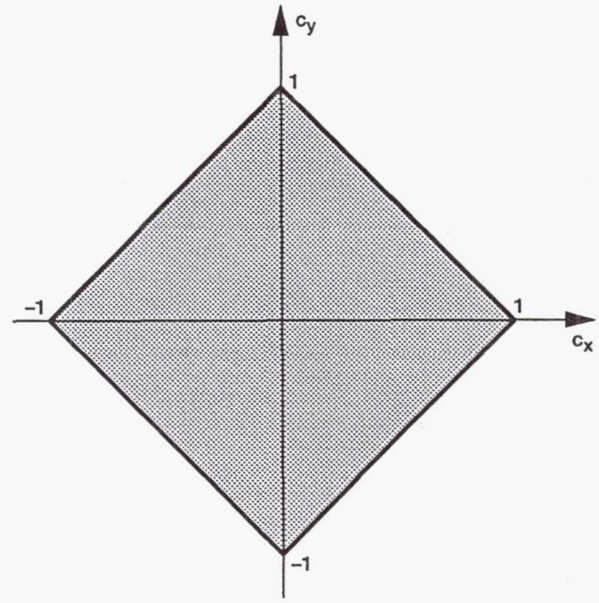

Figure 5.—Stability region (shaded) for the coordinate-wise first-order method. The scheme is stable for $|c_x| + |c_y| \leq 1$.

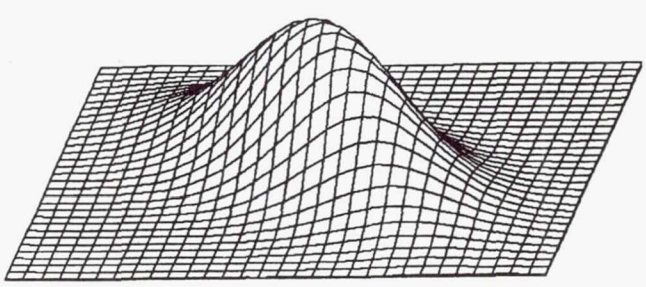

Figure 4.—Results for first-order upwinding used coordinate-wise for $\theta = 45°$; $c_x = c_y = 0.5$; N = 62, $\Delta t = \sqrt{2}/62$. $\phi_{max} = 0.473$; no undershoots.

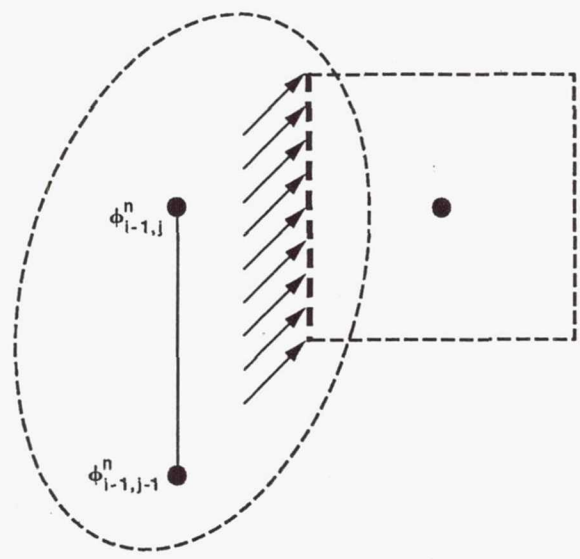

Figure 6.—Advective flux at an angle into the west face of a control volume, suggesting dependence on the transverse gradient.

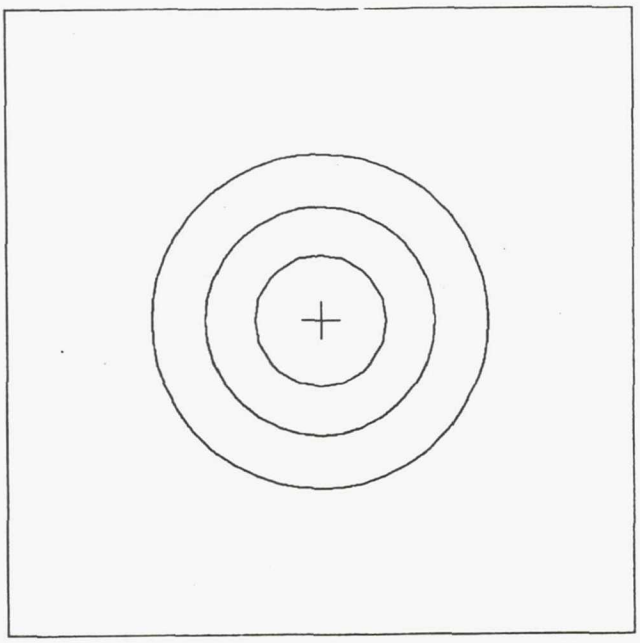

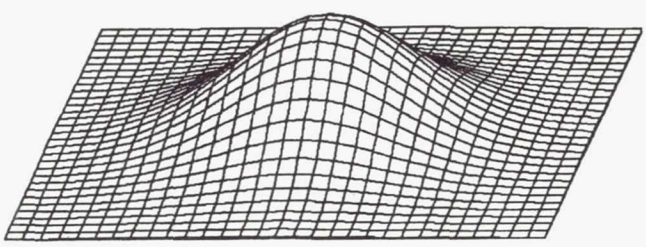

Figure 7.—Results for first-order upwinding including GRADT terms; $\theta = 45°$; $c_x = c_y = 0.5$; N = 62, $\Delta t = \sqrt{2}/62$. Note the good isotropy in comparison with Figure 4. $\phi_{max} = 0.366$; no undershoot.

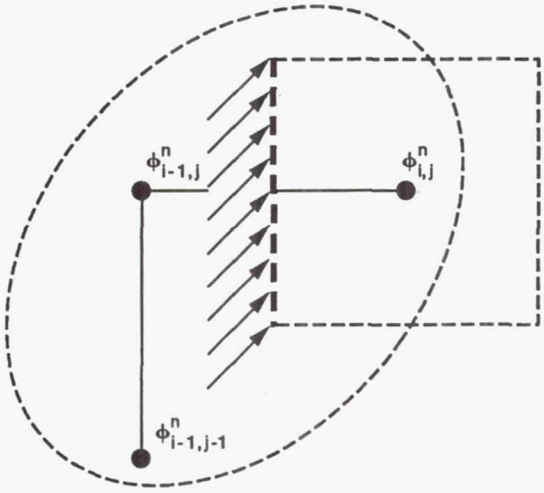

Figure 8.—Calculation of the time-averaged west-face value assuming a linear (x, y) dependence in the vicinity of the face, collocated at the three nodes shown (for c_x, $c_y > 0$).

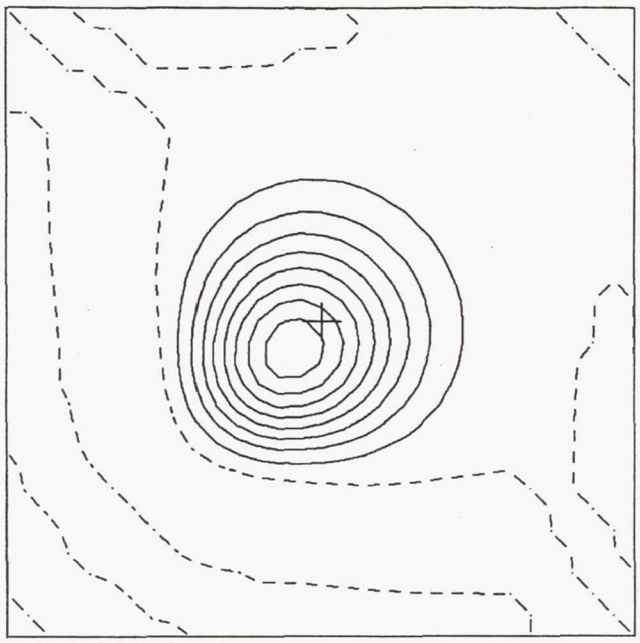

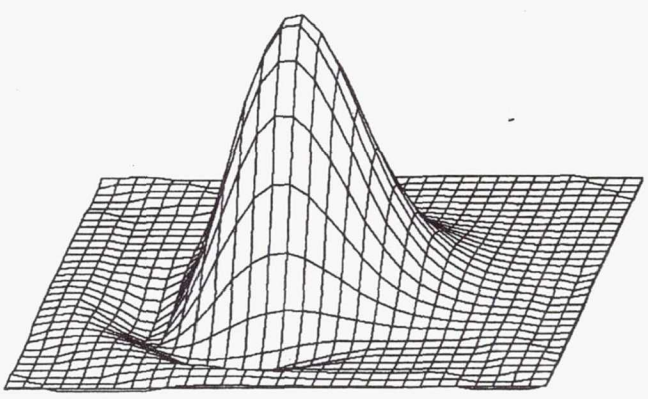

Figure 9.—Results of the generalised two-dimensional Lax-Wendroff scheme including GRADT terms; $\theta = 45°$; $c_x = c_y = 0.25$; N = 124, $\Delta t = \sqrt{2}/124$. $\phi_{max} = 0.867$, $\phi_{min} = -0.087$.

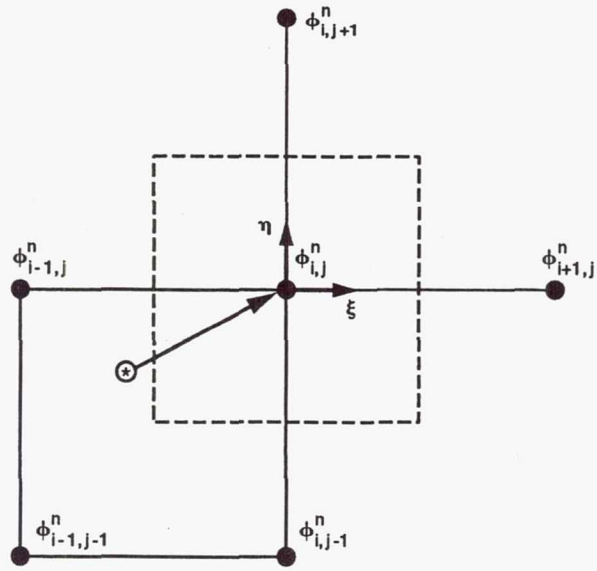

Figure 10.—Six-point stencil used for deriving the two-dimensional Lax-Wendroff scheme by back-tracking along an advective characteristic. Note the upwind bias (for the case shown, c_x, $c_y > 0$).

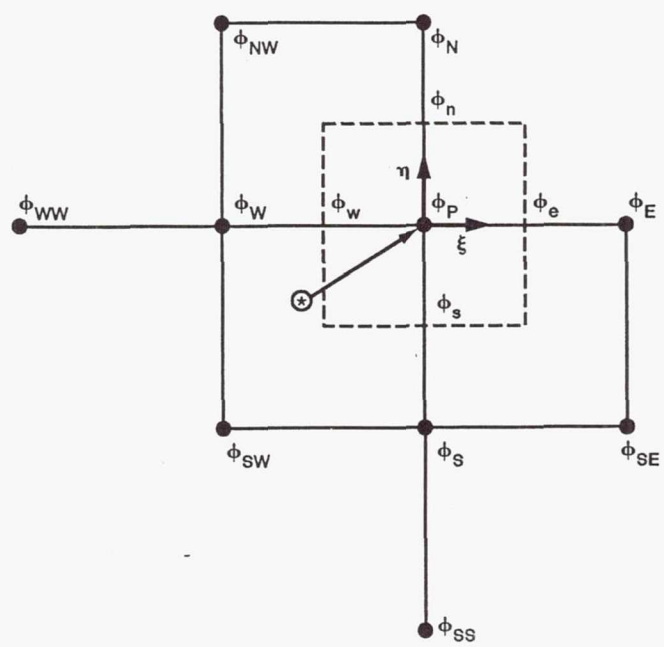

Figure 11.—Upwind-biased ten-point stencil used for the interpolation of $\phi^n(\xi, \eta)$ given by Equation (44).

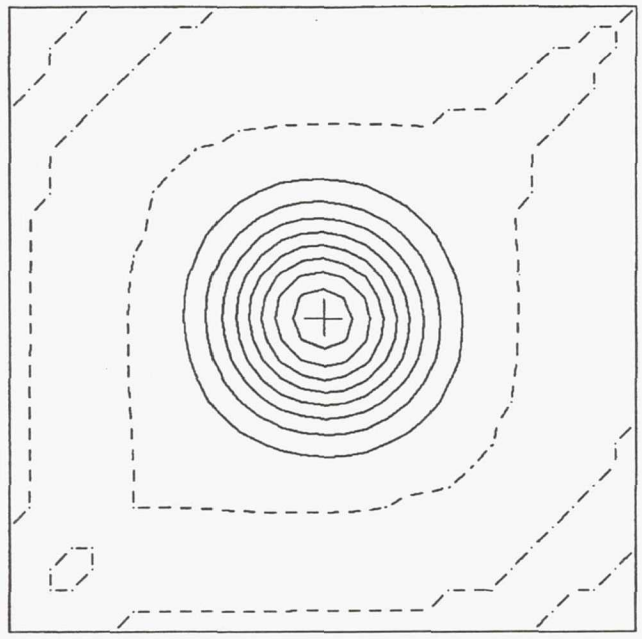

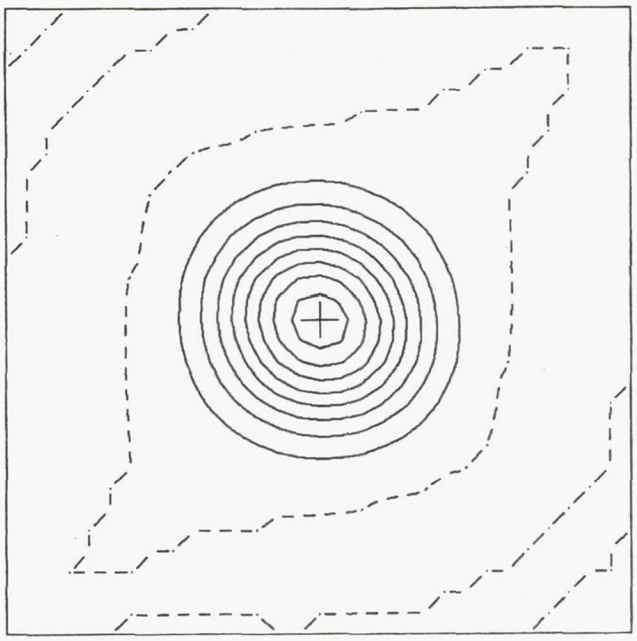

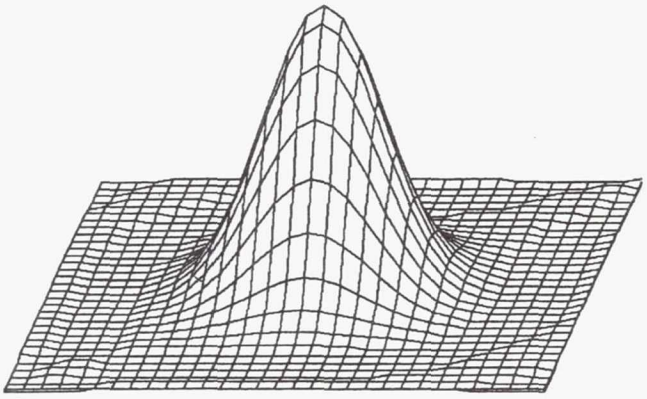

Figure 12.—Results for the uniformly third order polynomial interpolation algorithm (UTOPIA); $\theta = 45°$; $c_x = c_y = 0.25$; $N = 124$, $\Delta t = \sqrt{2}/124$. $\phi_{max} = 0.885$, $\phi_{min} = -0.004$. Note the good isotropy and phase accuracy.

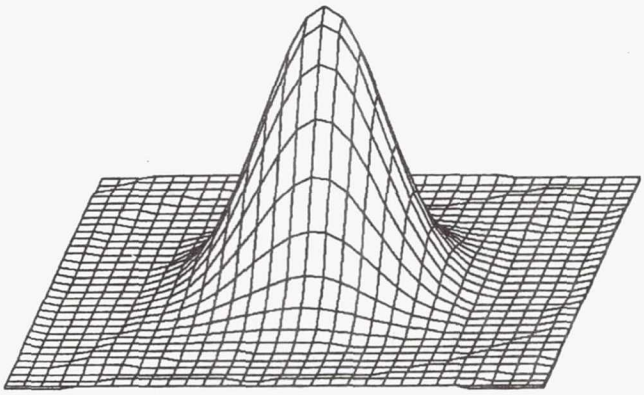

Figure 13.—UTOPIA results for $\theta = \tan^{-1}(1/2) \approx 26.565°$; $c_x = 0.5$, $c_y = 0.25$; $N = 124$, $\Delta t = \sqrt{5}/124$. $\phi_{max} = 0.872$, $\phi_{min} = -0.006$.

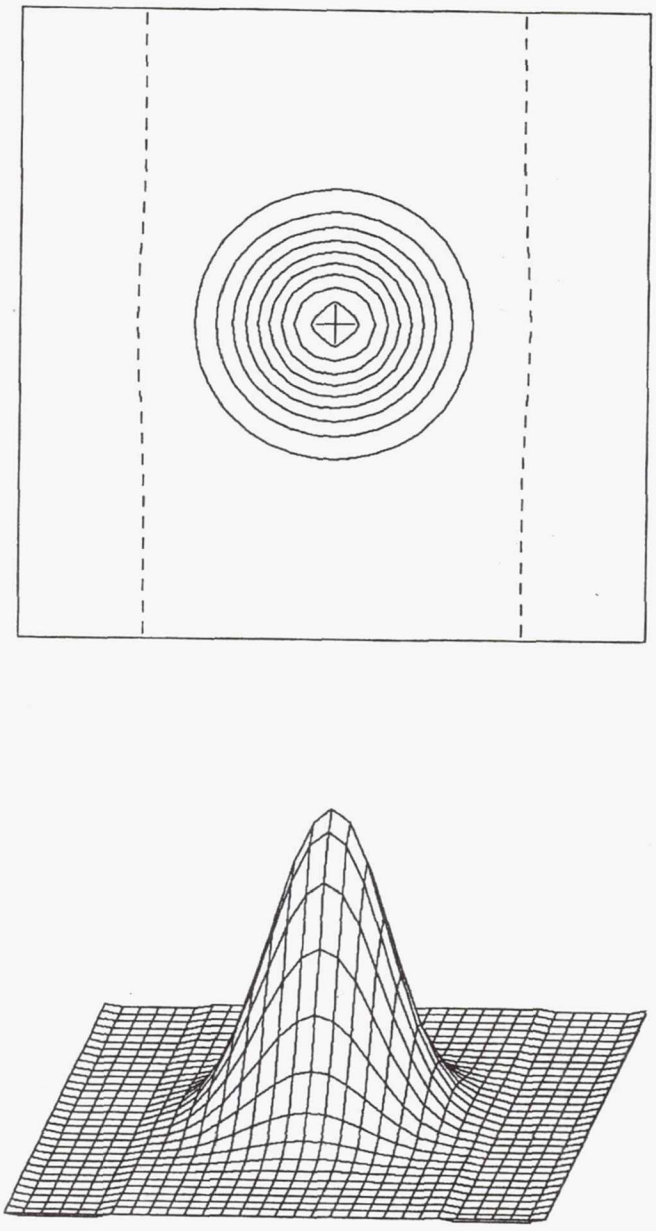

Figure 14.—UTOPIA results for $\theta = 0°$; $c_x = 0.5$, $c_y = 0$; N = 62, $\Delta t = 1/62$. $\phi_{max} = 0.958$, $\phi_{min} = -0.002$.

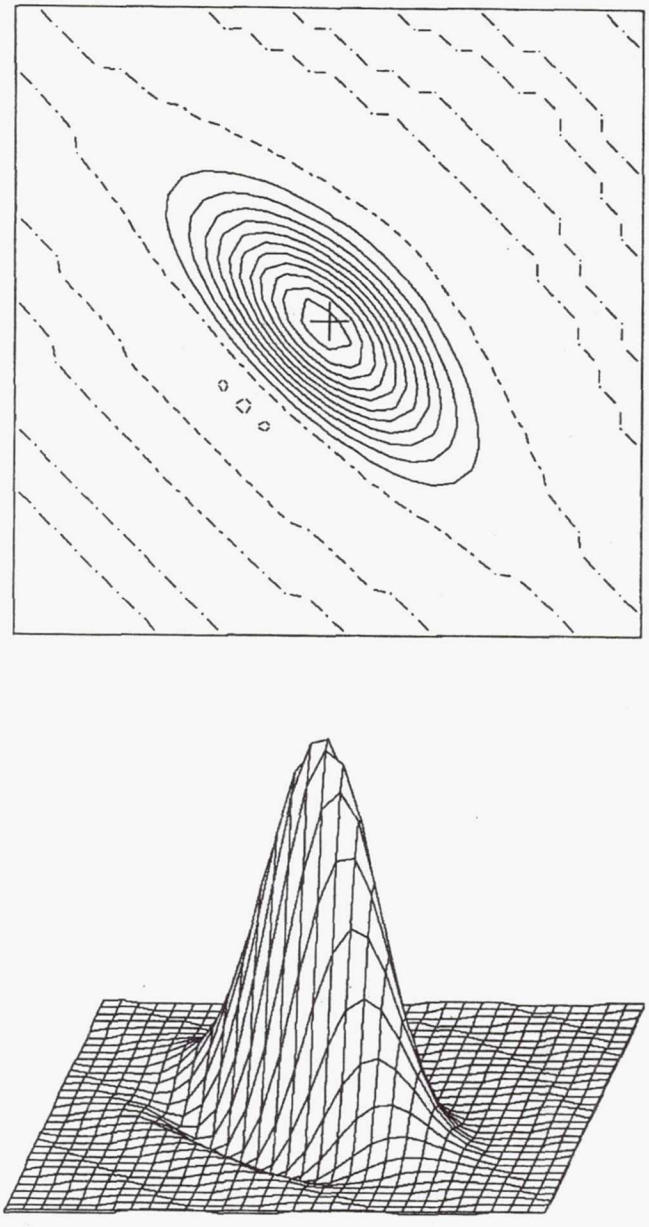

Figure 15.—Results using the one-dimensional QUICKEST scheme coordinate-wise (Davis & Moore's method) for $\theta = 45°$; $c_x = c_y = 0.25$; N = 124, $\Delta t = \sqrt{2}/124$. $\phi_{max} = 1.167$, $\phi_{min} = -0.111$.

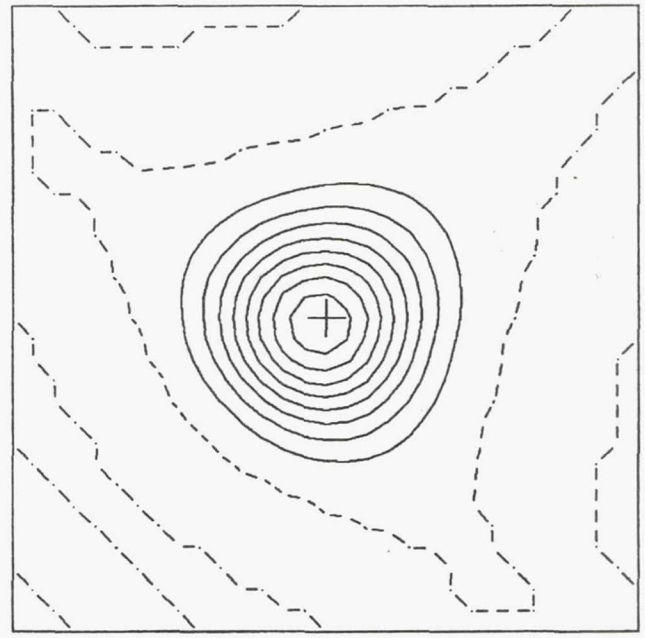

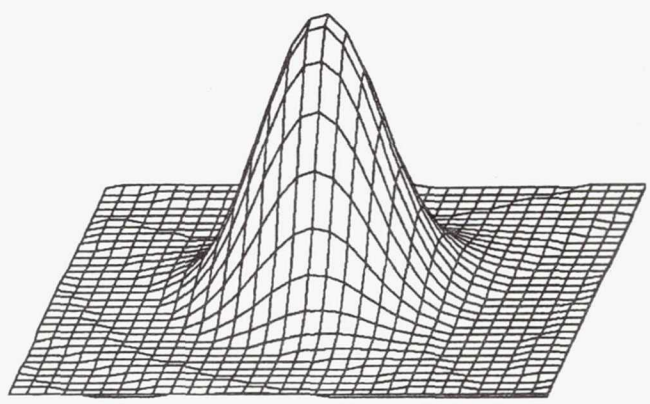

Figure 16.—"Quasi-third-order" method consisting of QUICKEST together with GRADT terms (only) for $\theta = 45°$; $c_x = c_y = 0.25$; $N = 124$, $\Delta t = \sqrt{2}/124$. $\phi_{max} = 0.880$, $\phi_{min} = -0.010$.

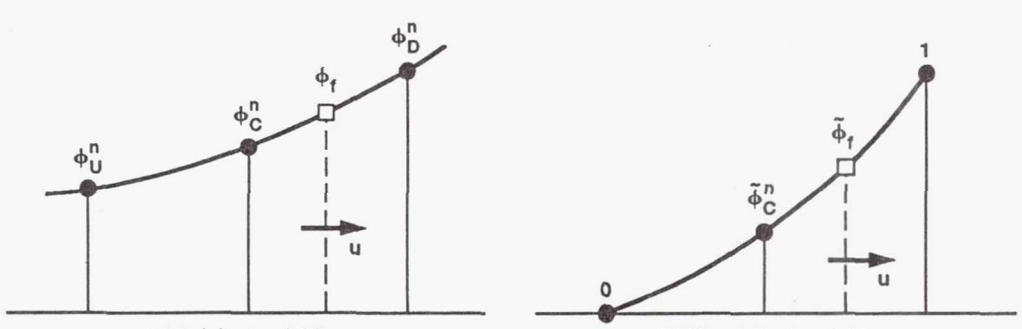

(a) Original variables.

(b) Normalized variables.

Figure 17.—Definition of geheric upwind (U), downwind (D), and central (C) node-values, depending on the sign of u.

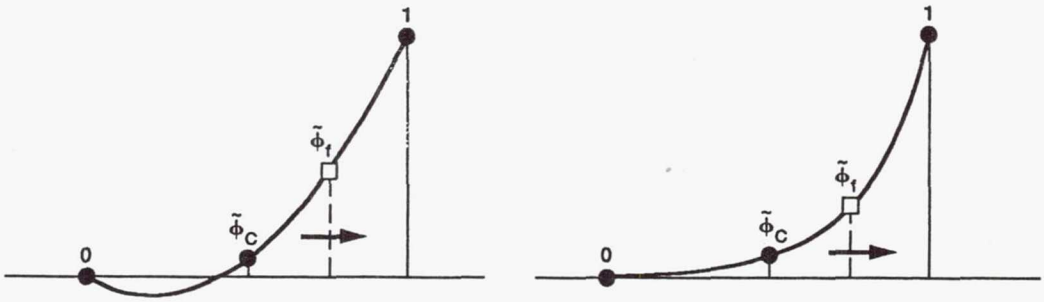

(a) Parabolic interpolation. (b) Exponential interpolation.

Figure 18.—Interpolation through the same three (normalised) node-values.

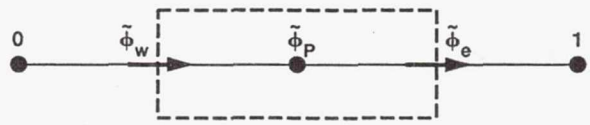

Figure 19.—Schematic one-dimensional control-volume showing east and west face-values.

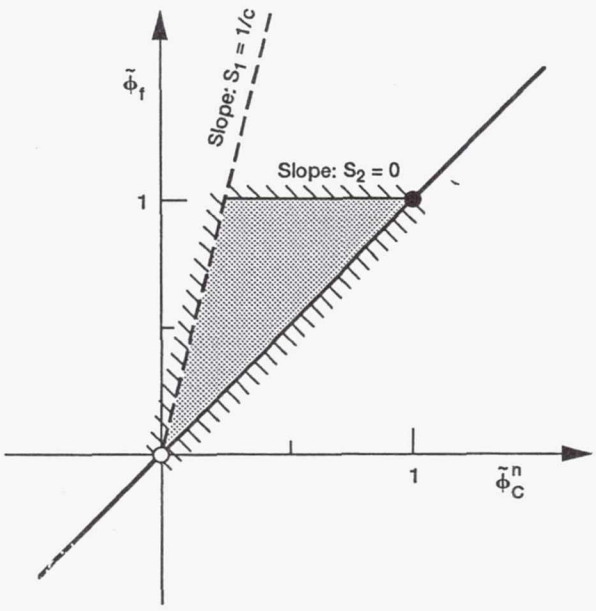

Figure 20.—One-dimensional universal limiter constraints corresponding to (63), (66), and (67). Note the slopes: $S_1 = 1/c$, and (for later reference) $S_2 = 0$. The case shown is for $c = 0.25$.

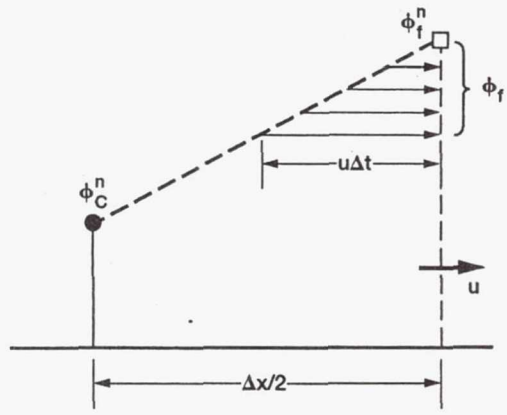

Figure 21.—Estimation of the time-averaged face-value, ϕ_f, assuming linear variation between ϕ_c^n and ϕ_f^n, and constant advecting velocity.

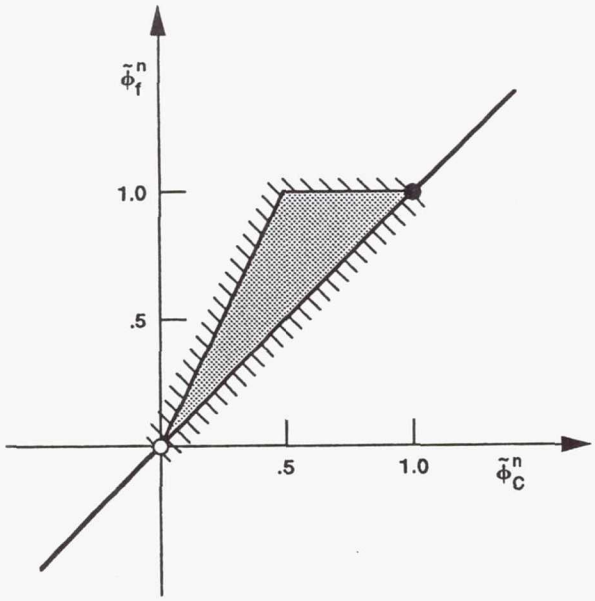

Figure 22.—TVD flux-limiter constraints in terms of $\tilde{\phi}_f^n$ vs. $\tilde{\phi}_C^n$.

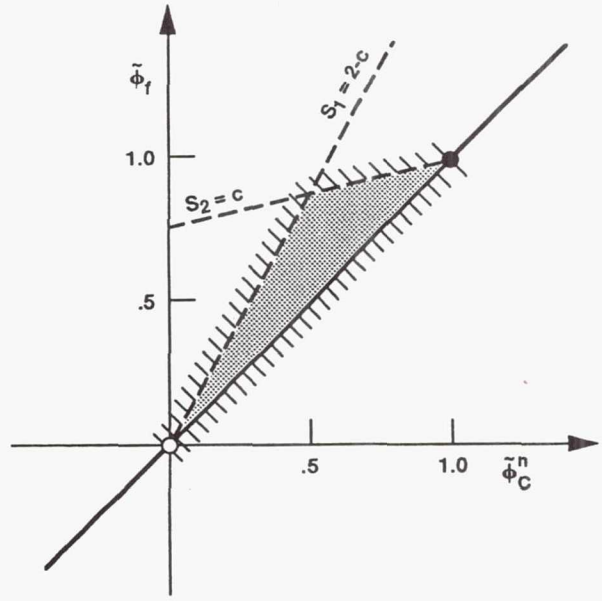

Figure 23.—TVD flux-limiter constraints in terms of $\tilde{\phi}_f$ vs. $\tilde{\phi}_C^n$. The case shown is for c = 0.25 (S_1 = 1.75, S_2 = 0.25).

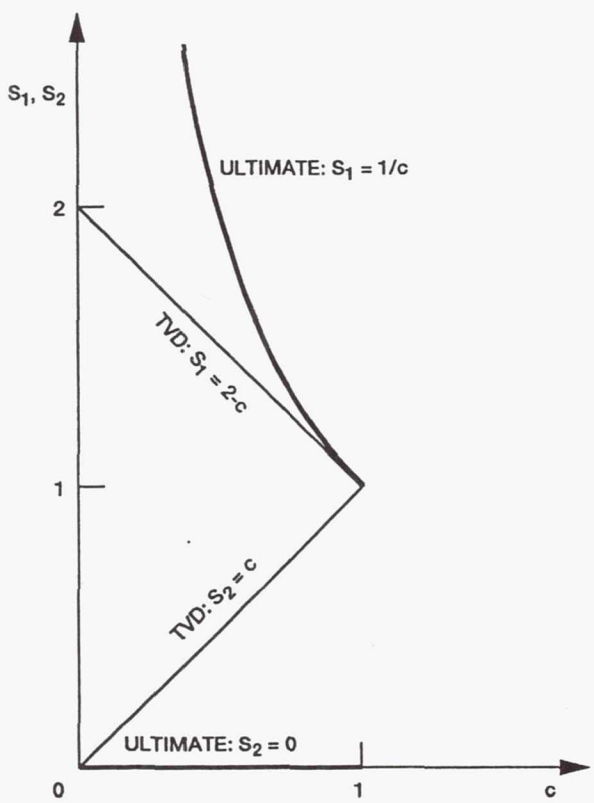

Figure 24.—Upper constraint slopes, S_1 and S_2, for ULTIMATE (heavy lines) and TVD schemes (light lines).

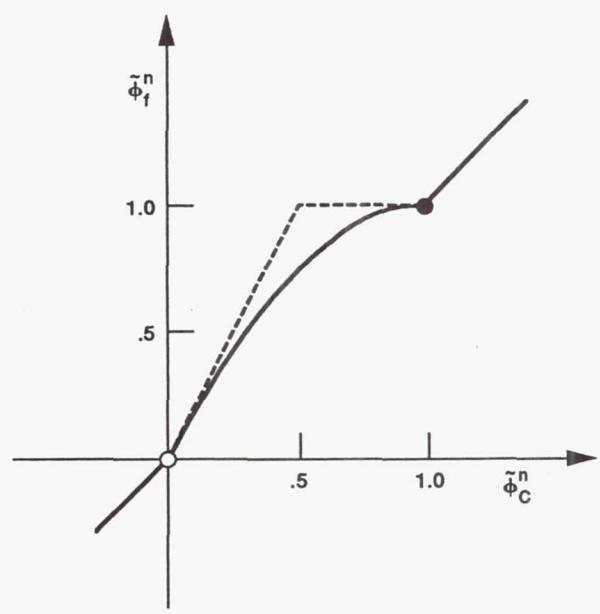

Figure 25.—One-dimensional TVD (CLAM) scheme of van Leer in the ($\tilde{\phi}_C^n$, $\tilde{\phi}_f^n$) plane.

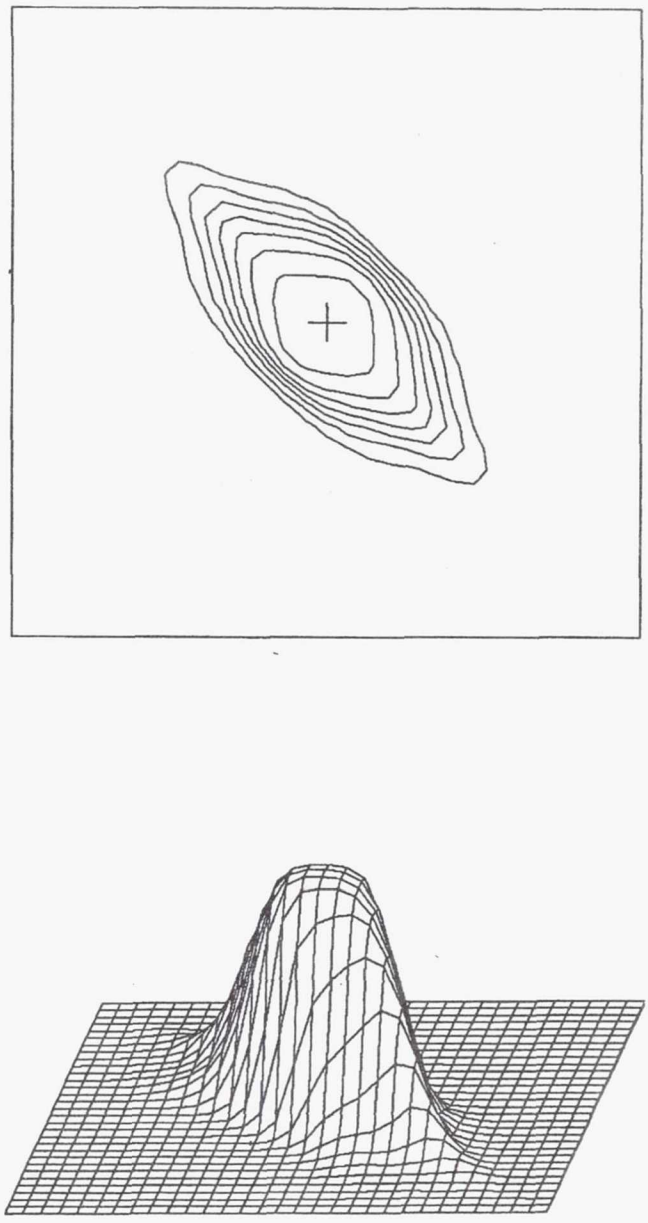

Figure 26.—Results using the one-dimensional TVD (CLAM) scheme coordinate-wise for $\theta = 45°$; $c_x = c_y = 0.25$; N = 124, $\Delta t = \sqrt{2}/124$. $\phi_{max} = 0.754$, no undershoot.

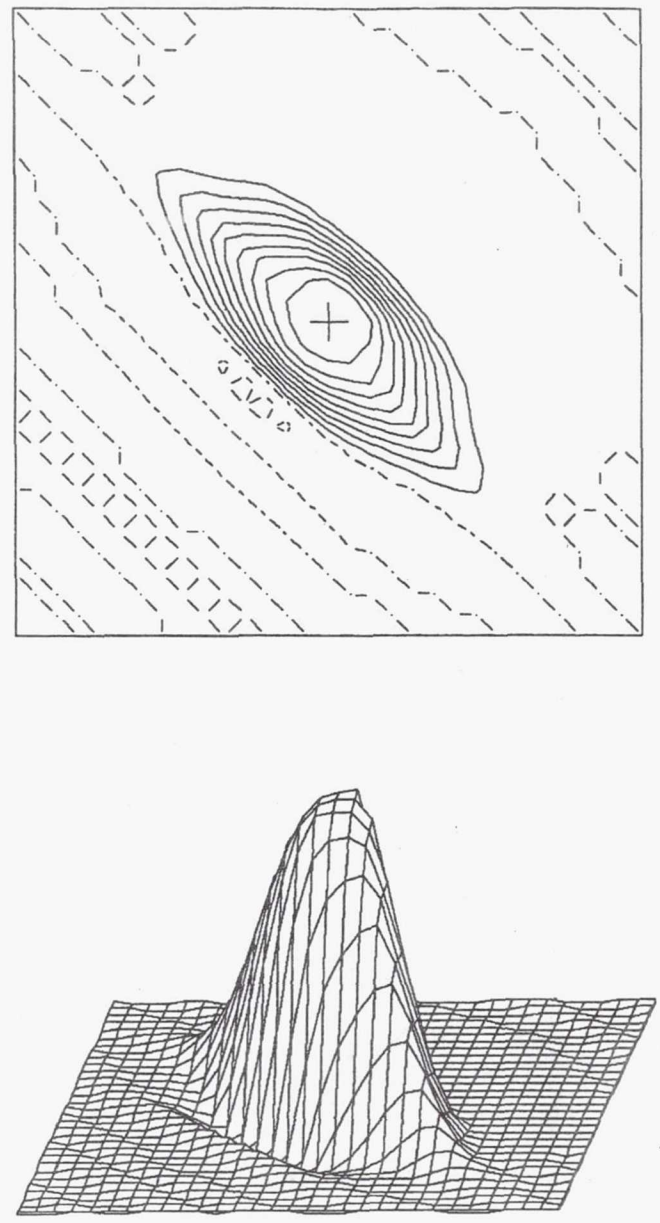

Figure 27.—One-dimensional ULTIMATE QUICKEST scheme used coordinate-wise for $\theta = 45°$; $c_x = c_y = 0.25$; N = 124, $\Delta t = \sqrt{2}/124$. $\phi_{max} = 0.985$, $\phi_{min} = -0.124$.

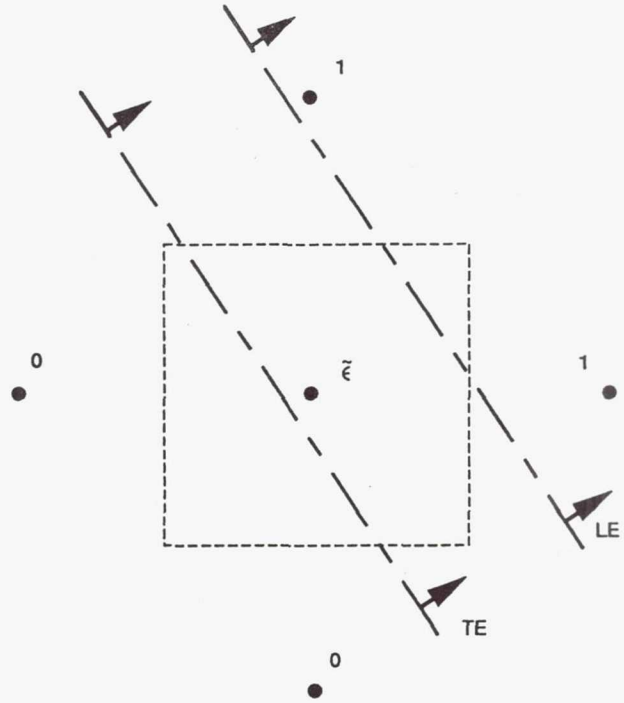

Figure 28.—Normalised "front" passing obliquely through a control volume.

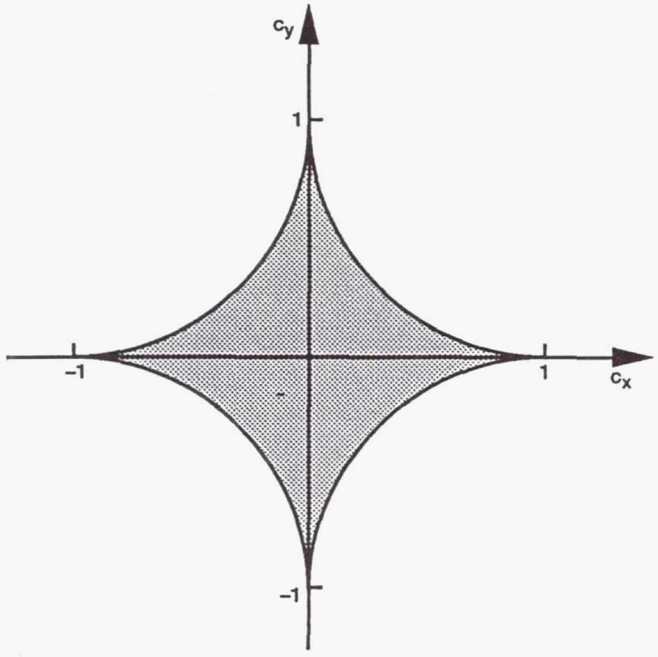

Figure 29.—Restriction on the allowable component Courant numbers for positivity-preserving schemes using TVD limiters in each coordinate direction. Boundaries are quarter-circles with centres at (±1, ±1).

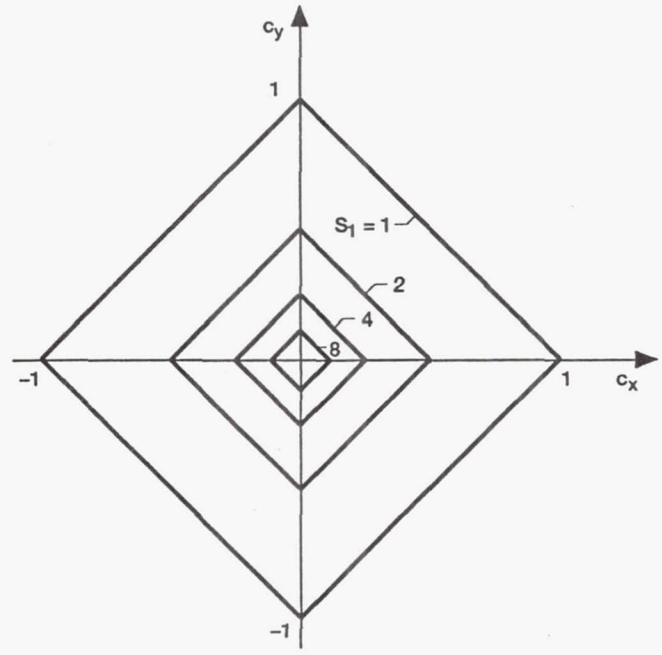

Figure 30.—Contours in the (c_x, c_y) plane of the first 2D limiter slope, S_1, according to Equation 97.

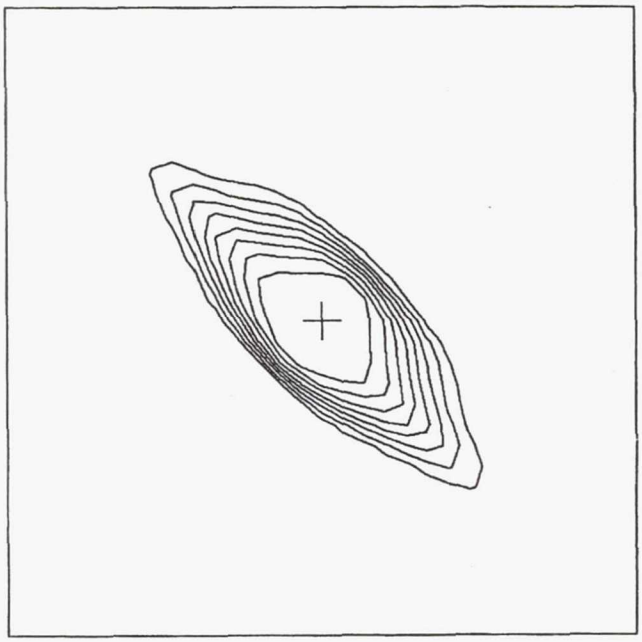

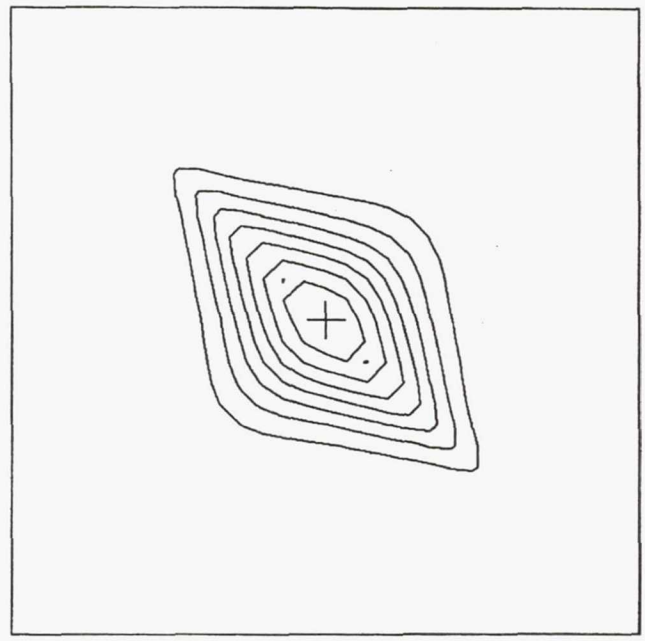

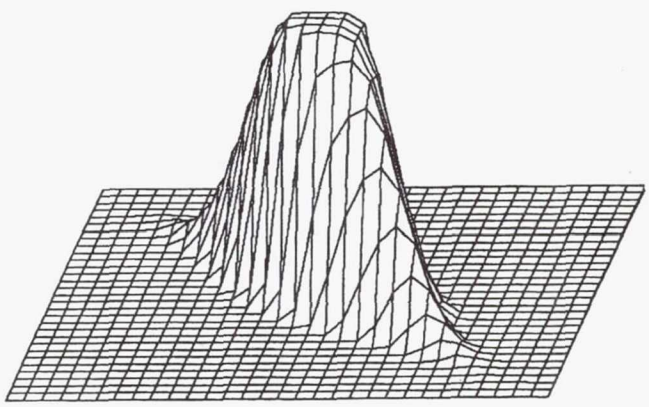

Figure 31.—Two-dimensional limiter of (97) applied to the QUICKEST scheme used coordinate-wise for $\theta = 45°$; $c_x = c_y = 0.25$; N = 124, $\Delta t = \sqrt{2}/124$. $\phi_{max} = 0.874$, no undershoot.

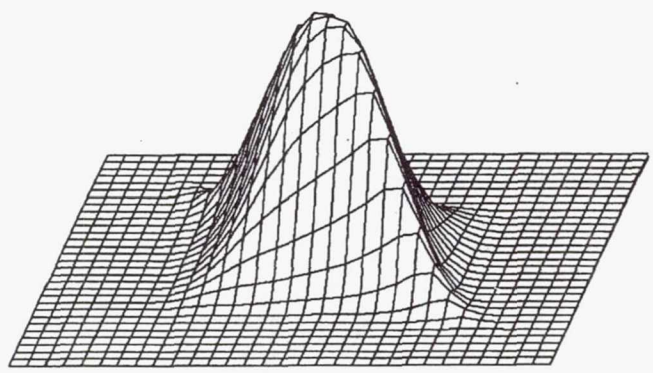

Figure 32.—The two-dimensional limiter of (97) applied to UTOPIA for $\theta = 45°$; $c_x = c_y = 0.25$; N = 124, $\Delta t = \sqrt{2}/124$. $\phi_{max} = 0.777$, no undershoot.

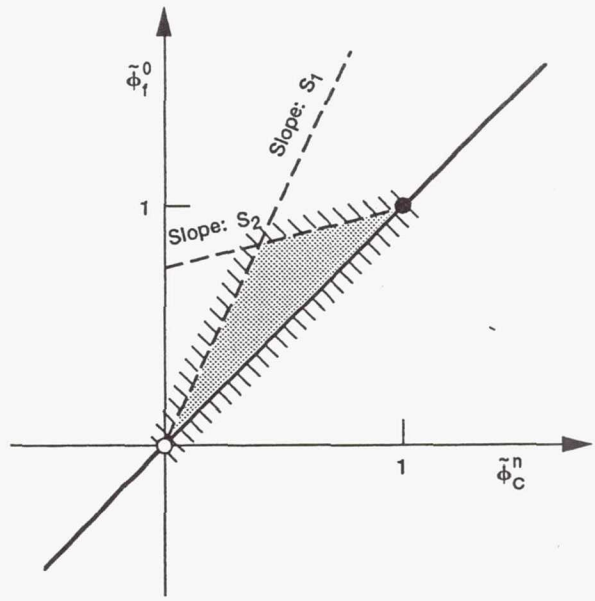

Figure 33.—Second two-dimensional limiter portrayed in the $(\tilde{\phi}_c^n, \tilde{\phi}_f^0)$ plane, according to (119) and (120). The case shown is for $c_x = c_y = 0.25$ ($S_1 = 2.125$, $S_2 = 0.25$).

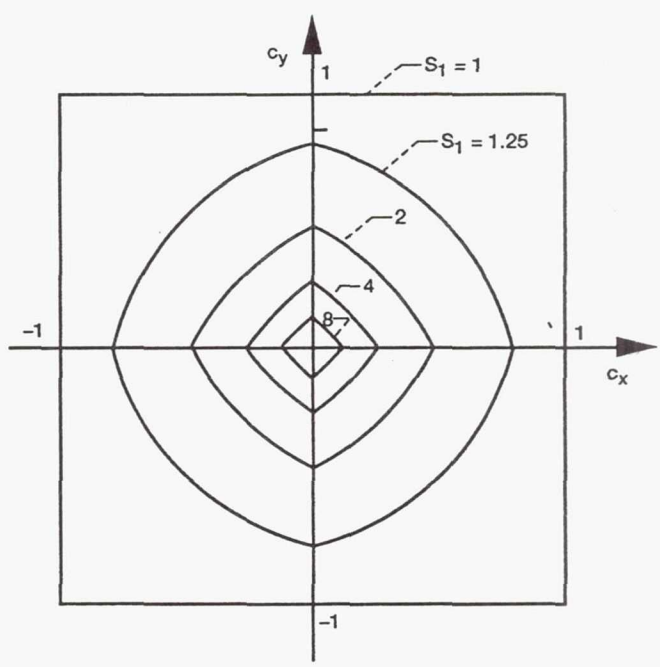

Figure 34.—Contour lines of S_1 according to (130). Note the "flat" regions ($S_1 \rightarrow 1$) towards the corners of the diagram.

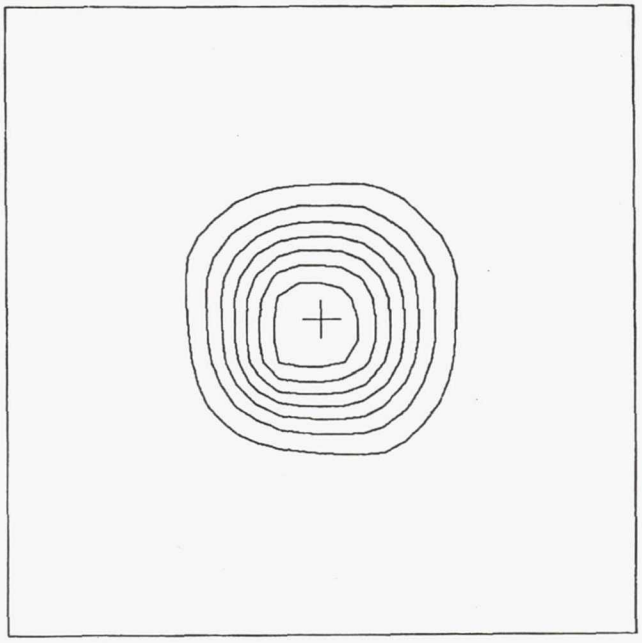

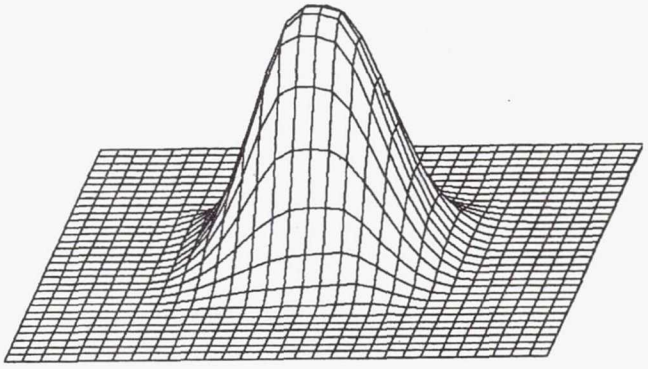

Figure 35.—The two-dimensional limiter of (130), (131) applied to UTOPIA for $\theta = 45°$; $c_x = c_y = 0.25$; $N = 124$, $\Delta t = \sqrt{2}/124$. $\phi_{max} = 0.782$, no undershoot.

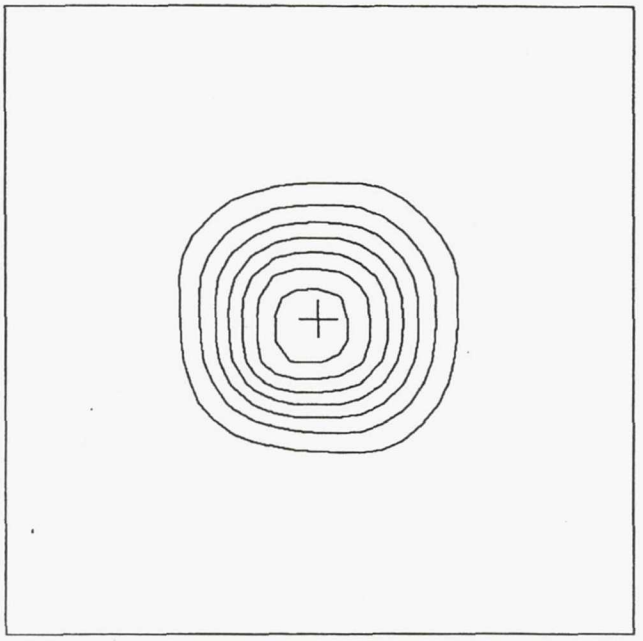

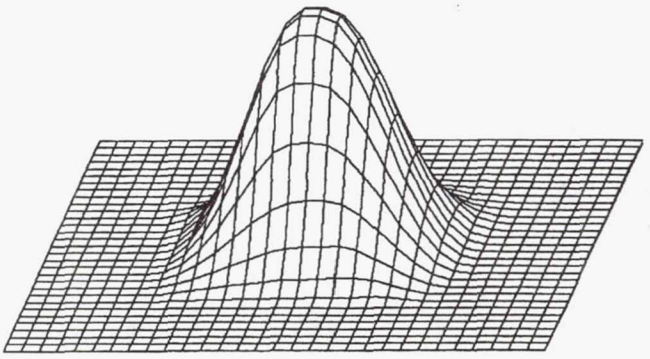

Figure 36.—The two-dimensional limiter of (130), (131) applied to UTOPIA for $\theta = \tan^{-1}(1/2) \approx 26.565°$; $c_x = 0.25$, $c_y = 0.125$; $N = 248$, $\Delta t = \sqrt{5}/248$. $\phi_{max} = 0.752$, no undershoot.

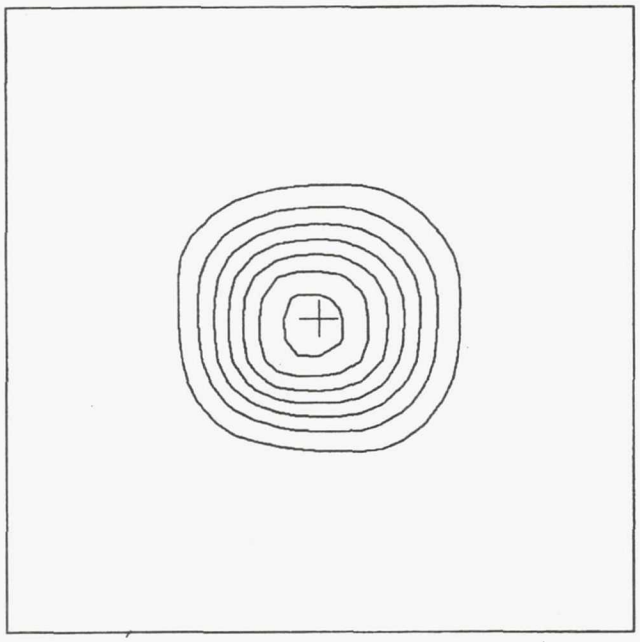

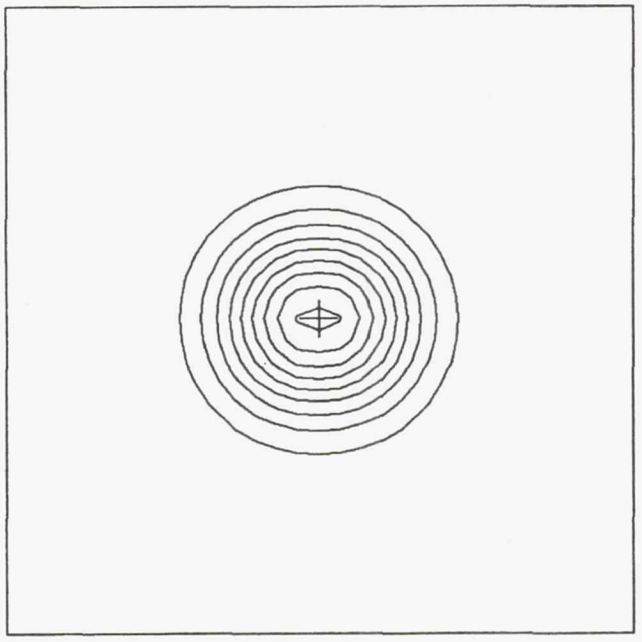

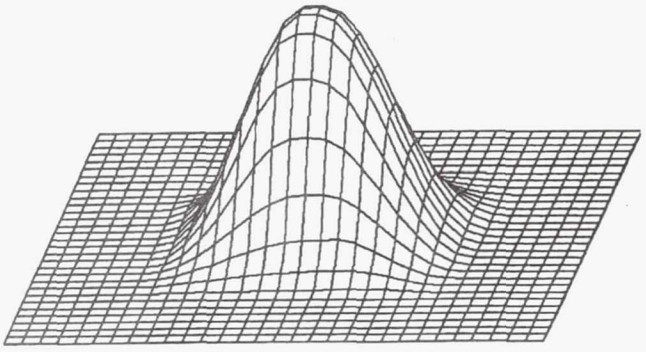

Figure 37.—The two-dimensional limiter of (130), (131) applied to UTOPIA for $\theta = \tan^{-1}(1/3) \approx 18.435°$; $c_x = 0.25 = 3\,c_y$; N = 372, $\Delta t = \sqrt{10}/372$. $\phi_{max} = 0.731$, no undershoot.

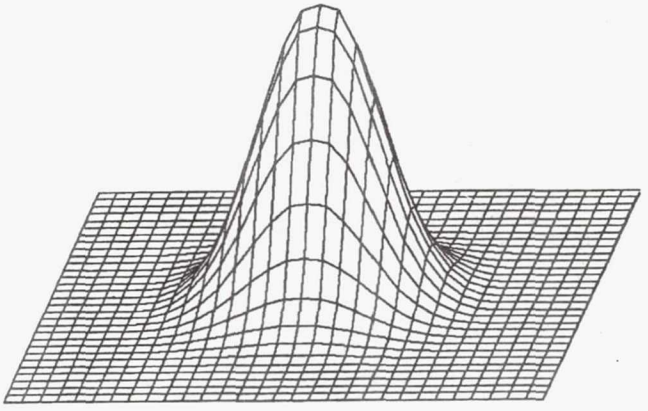

Figure 38.—The two-dimensional limiter of (130), (131) applied to UTOPIA for $\theta = 0°$; $c_x = 0.5$, $c_y = 0$; N = 62, $\Delta t = 1/62$. $\phi_{max} = 0.927$, no undershoot.

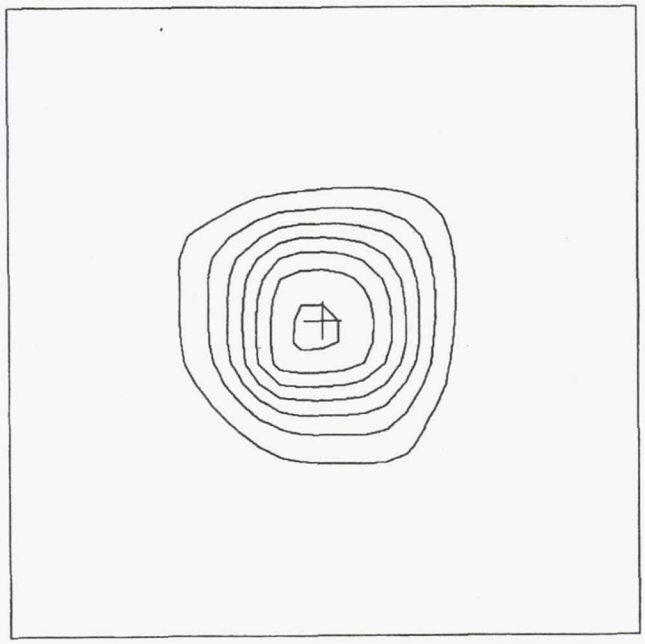

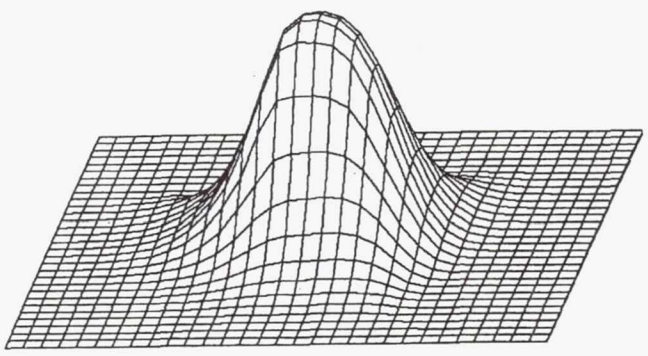

Figure 39.—The two-dimensional limiter of (130), (131) applied to UTOPIA for $\theta = 45°$; $c_x = c_y = 0.5$; N = 62, $\Delta t = \sqrt{2}/62$. $\Phi_{max} = 0.715$, no undershoot.

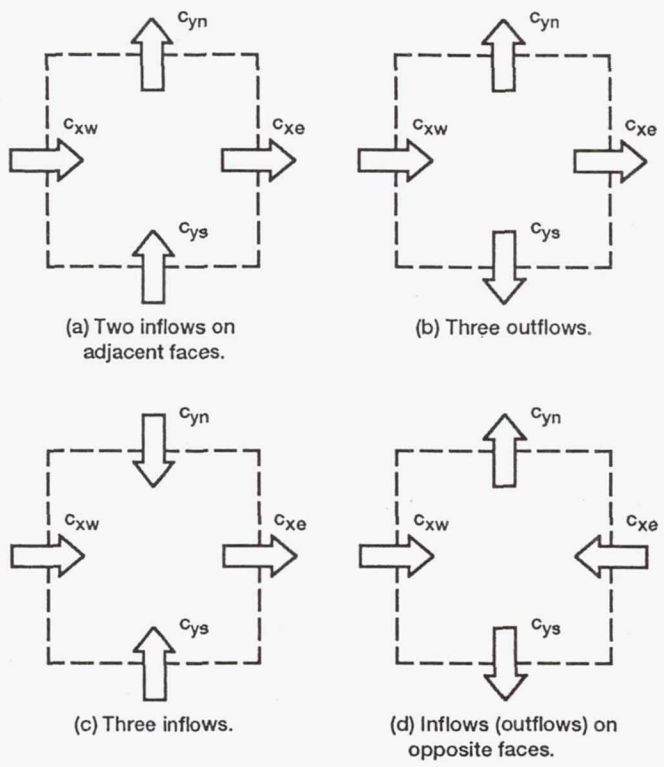

(a) Two inflows on adjacent faces.

(b) Three outflows.

(c) Three inflows.

(d) Inflows (outflows) on opposite faces.

Figure 40.—Four inflow-outflow configurations.

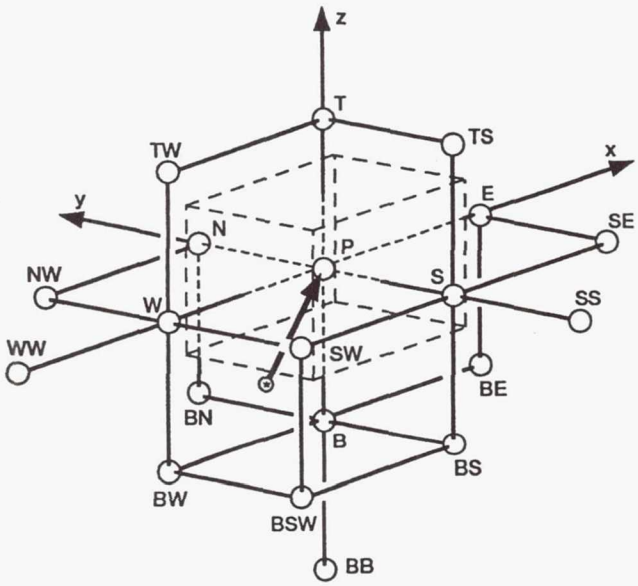

Figure A.1.1.—Twenty-node three-dimensional molecule for third-order upwinding. For the case shown, c_x, c_y, c_z >0.

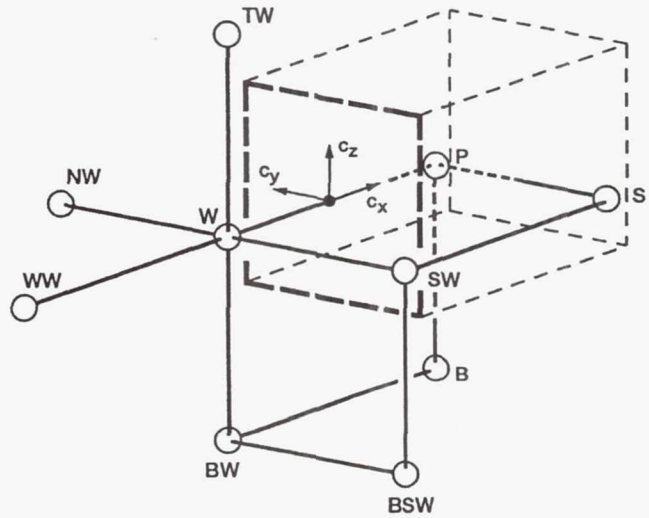

Figure A.1.2.—Upwind-biased ten-node molecule used for computing the west-face advected value. The case shown is for c_x, c_y, c_z >0.

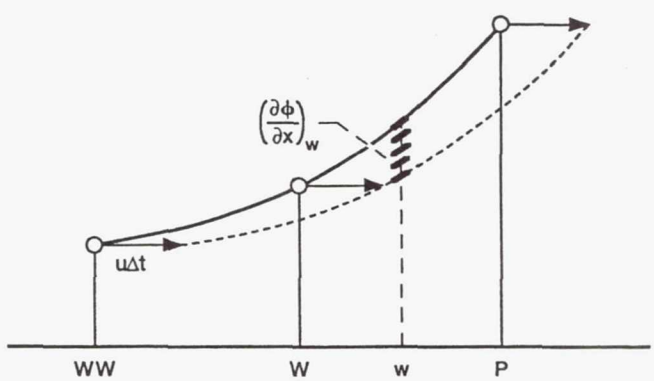

Figure A.2.1.—Variation of the normal gradient at the west face due to curvature in the advected profile.

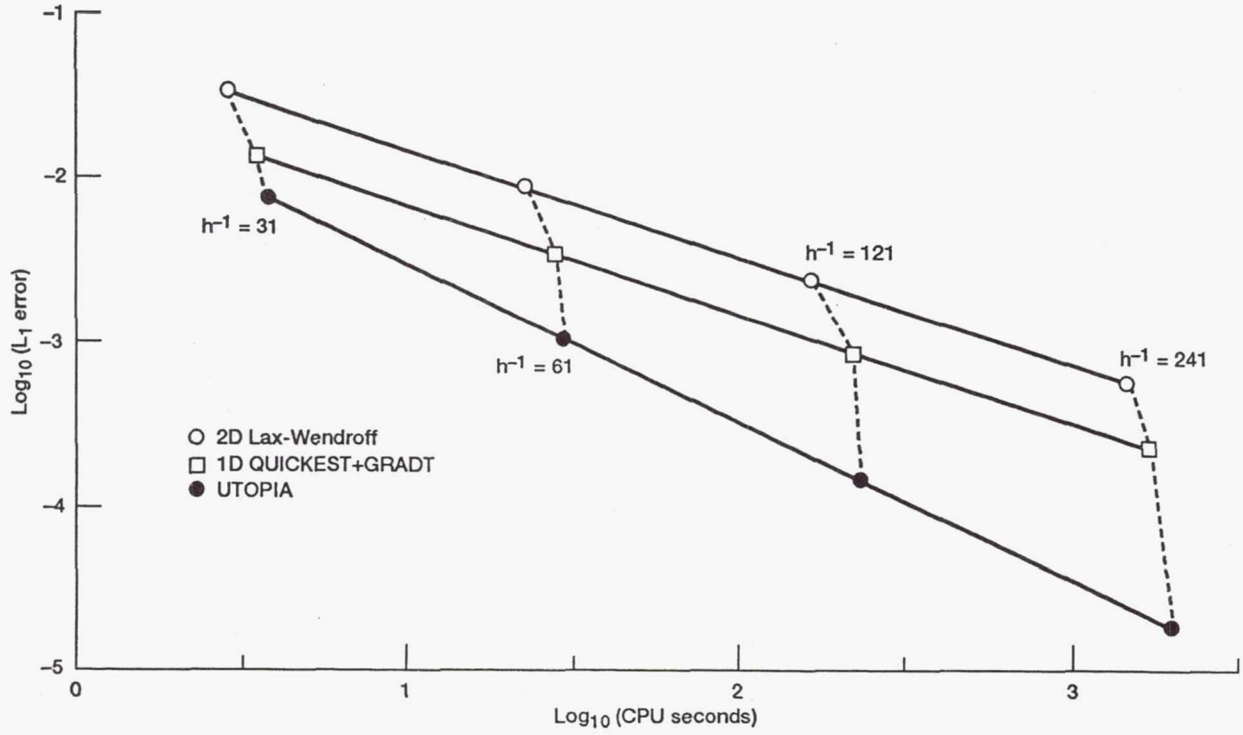

Figure A.3.1.—Computational efficiency diagram (error versus cost, on a log-log scale) for the two-dimensional generalised Lax-Wendroff scheme, the one-dimensional QUICKEST scheme used coordinate-wise together with transverse-gradient terms, and the uniformly third-order polynominal interpolation algorithm (UTOPIA).

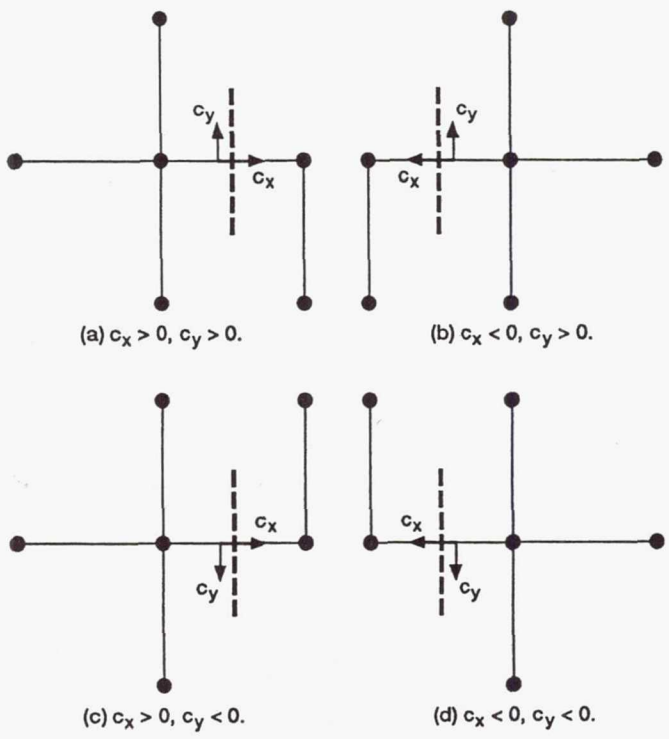

Figure A.6.1.—Four possible two-dimensional stencils depending on the signs of the velocity components at the face in question.

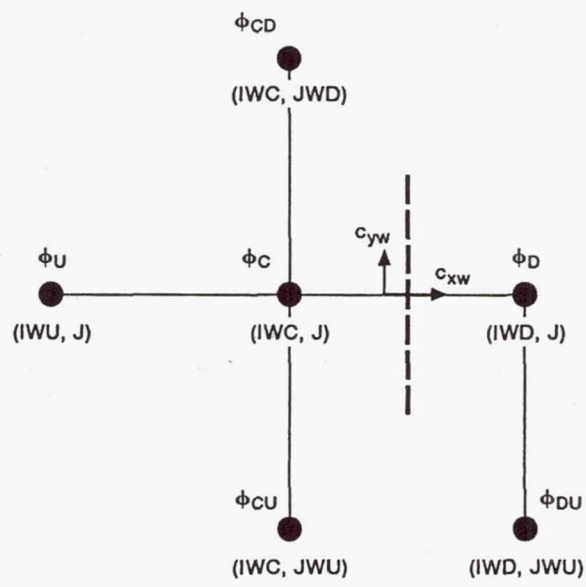

Figure A.6.2.—Generic two-dimensional stencil for the west face of the control volume.

REPORT DOCUMENTATION PAGE

Form Approved
OMB No. 0704-0188

1. AGENCY USE ONLY (*Leave blank*)

2. REPORT DATE
March 1993

3. REPORT TYPE AND DATES COVERED
Technical Memorandum

4. TITLE AND SUBTITLE
Positivity-Preserving Numerical Schemes for Multidimensional Advection

5. FUNDING NUMBERS
WU–505–90–5K

6. AUTHOR(S)
B.P. Leonard, M.K. MacVean, and A.P. Lock

7. PERFORMING ORGANIZATION NAME(S) AND ADDRESS(ES)
National Aeronautics and Space Administration
Lewis Research Center
Cleveland, Ohio 44135–3191

8. PERFORMING ORGANIZATION REPORT NUMBER
E–7656

9. SPONSORING/MONITORING AGENCY NAMES(S) AND ADDRESS(ES)
National Aeronautics and Space Administration
Washington, D.C. 20546–0001

10. SPONSORING/MONITORING AGENCY REPORT NUMBER
NASA TM–106055
ICOMP–93–05

11. SUPPLEMENTARY NOTES
B.P. Leonard, Institute for Computational Mechanics in Propulsion, Lewis Research Center (work funded under NASA Cooperative Agreement NCC3–233), M.K. MacVean and A.P. Lock, U.K. Meteorological Office, Atmospheric Processes Research Division, Bracknell, England. ICOMP Program Director, Louis A. Povinelli (216) 433–5818.

12a. DISTRIBUTION/AVAILABILITY STATEMENT
Unclassified - Unlimited
Subject Category 34

12b. DISTRIBUTION CODE

13. ABSTRACT ***(Maximum 200 words)***

This report describes the construction of an explicit, single time-step, conservative, finite-volume method for multidimensional advective flow, based on a uniformly third-order polynomial interpolation algorithm (UTOPIA). Particular attention is paid to the problem of flow-to-grid angle-dependent, anisotropic distortion typical of one-dimensional schemes used component-wise. The third-order multidimensional scheme automatically includes certain cross-difference terms that guarantee good isotropy (and stability). However, above first-order, polynomial-based advection schemes do not preserve positivity (the multidimensional analogue of monotonicity). For this reason, a multidimensional generalisation of the first author's universal flux-limiter is sought. This is a very challenging problem. A simple flux-limiter can be found; but this introduces strong anisotropic distortion. A more sophisticated technique, limiting part of the flux and then restoring the isotropy-maintaining cross-terms afterwards, gives more satisfactory results. Test cases are confined to two dimensions; three-dimensional extensions are briefly discussed.

14. SUBJECT TERMS
Multidimensional advection; Computational fluid dynamics; Flux limiters; Positivity preservation

15. NUMBER OF PAGES
62

16. PRICE CODE
A04

17. SECURITY CLASSIFICATION OF REPORT
Unclassified

18. SECURITY CLASSIFICATION OF THIS PAGE
Unclassified

19. SECURITY CLASSIFICATION OF ABSTRACT
Unclassified

20. LIMITATION OF ABSTRACT